Received: 18 July 2023 | Revised: 7 October 2023 | Accepted: 24 October 2023

IET Radar, Sonar & Navigation

DOI: 10.1049/rsn2.12504

The Institution of Engineering and Technology WILEY

ORIGINAL RESEARCH

On the anti-intercept features of noise radars

Gaspare Galati[1,2] | Gabriele Pavan[1,2]

[1]Department of Electronic Engineering, Tor Vergata University, Rome, Italy

[2]CNIT (National Inter-University Consortium for Telecommunications) Research Unit of Tor Vergata University, Rome, Italy

Correspondence

Gabriele Pavan.
Email: gabriele.pavan@uniroma2.it

Abstract

Robustness against Electronic Warfare/Electronic Defence attacks represents an important advantage of Noise Radar Technology (NRT). An evaluation of the related Low Probability of Detection (LPD) and of Intercept (LPI) is presented for Continuous Emission Noise Radar (CE-NR) waveforms with different operational parameters, that is, "tailored", and with various "degrees of randomness". In this frame, three different noise radar waveforms, a phase Noise (APCN) and two "tailored" noise waveforms (FMeth and COSPAR), are compared by time–frequency analysis. Using a correlator (i.e. a two antennas) receiver, assuming a complete knowledge of the band (B) and duration (T) of the coherent emission of these waveforms, it will be shown that the LPD features of a CE-NR do not significantly differ from those of any CE radar transmitting deterministic waveforms. However, in real operations, B and T are unknown; hence, assuming an instantaneous bandwidth estimation will show that the duration T can be estimated only for some specific "tailored" waveforms (of course, not to be operationally used). The effect of "tailoring" is analysed with prospects for future work. Finally, some limitations in the classification of these radar signals are analysed.

KEYWORDS

electronic warfare, LPI radar, radar waveforms

1 | INTRODUCTION

1.1 | Operational frame and scope of this paper

In the Electronic Defence (ED) arena [1–4], an opponent could observe, record and exploit the victim's radar signal by Electronic Support Measurement (ESM) and/or Electronic Intelligence (ELINT) systems. To react against this situation, suited radar signals must be designed and transmitted in order to guarantee three levels of protection [5]:

(a) The signal must be difficult to be detected, that is, has to guarantee a Low Probability of Detection (LPD).
(b) When the signal has been detected, the estimation of its parameters must be hard, that is, the signal has to guarantee a Low Probability of Intercept (LPI).
(c) When intercepted, the signal must be protected from the exploitation of its features by an opponent, that is, has to guarantee Low Probability of Exploitation (LPE).

After a review of the state of art in the Noise Radar (NR) field, the main aims of this paper are as follows.

Abbreviations: 2A&C, two antennas and correlator; ADC, Analog-to-Digital Converter; AI, Artificial Intelligence; AM, Amplitude Modulation; APCN, Advanced Pulse Compression Noise; BT, Bandwidth–Time product; CE, Continuous Emission; CNN, Convolution Neural Networks; COSPAR, COmbined Spectral-shaping and Peak-to-Average power ratio Reduction; CPI, Coherent Processing Interval; CRS, Carrier Radar Signals; ED, Electronic Defence; ED, Energy Detector; ELINT, Electronic Intelligence; ESM, Electronic Support Measurement; FFT, Fast Fourier Transform; FM, Frequency Modulation; FM-CW, Frequency Modulation Continuous Wave; FMeth, Filtering Method; FPGA, Field Programmable Gate Arrays; HNLFM, Hybrid-Non-Linear-FM; HT, Hough Transform; IFFT, Inverse-Fast Fourier Transform; ISAC, Integrated Sensing and Communications; LFM, Linear Frequency Modulation; LPD, Low Probability of Detection; LPE, Low Probability of Exploitation; LPI, Low Probability of Intercept; LSTM, Long Short-Term Memory; MIMO, Multiple Input, Multiple Output; MOP, Modulation on Pulse; MTD, Moving Target Detector; NLFM, Non-Linear Frequency Modulation; NR, Noise Radar; NRT, Noise Radar Technology; PAPR, Peak to Average Power Ratio; PDM, Pulse Description Message; PDW, Pulse Description Word; PRI, Pulse Repetition Interval; PRNG, Pseudo Random Number Generators; PSL, Peak Sidelobes Level; PSWVD, Pseudo-Smoothed Wigner–Ville Distribution; SFM, Spectral Flatness Measure; SIGINT, Signal Intelligence; SLS, SideLobes-Suppression; SNR, Signal-to-Noise Ratio; SOI, Signal of interest; SVM, Support Vector Machines; TF, Time–Frequency; TFD, Time–Frequency Distribution; WPT, Wavelet Packet Transform; WVD, Wigner–Ville Distribution.

- The generation methods of *"tailored"* Continuous Emission (CE) Noise Radar (CE-NR) signals are able to improve the radar waveform features, that is, low Peak-to-Average Power Ratio (PAPR), good Peak Sidelobes Level (PSL), band occupancy, without degrading their robustness against detection, interception and exploitation. This is shown in the ensuing section 2.
- To analyse the LPD features of a CE-NR versus those of any conventional radar (deterministic signals) if a "*correlator*" type receiver (i.e. a 2 antennas) is used (section 3). Ideal conditions for intercept are supposed, that is, (i) absence of overlapping signals and (ii) knowledge of the duration T of the coherence period of the waveform and of its bandwidth occupation (from $f_0 - \frac{B}{2}$ to $f_0 + \frac{B}{2}$).
- To consider that the knowledge of B and T may be very hard and may be rendered harder by suitable resign of the own NR emission, including agility (i.e. pseudorandom variation) of B and T, mimicking the agility of central frequency and of pulse repetition interval (PRI) of military pulse radars. A possible estimation of B and T by the time–frequency analysis is shown in section 4.
- Some limitations of the today widely used recognition and classification methods for radar signals are shown in section 5.

1.2 | LPI/LPD waveforms and Continuous-Emission Noise Radar

In principle, LPD/LPI features can be reached by spreading the signal energy over a wide bandwidth B for a relative long time T less or equal to T_{Dwell}, where T_{Dwell} is the time-on-target (or Dwell-Time). In doing so, the theoretical maximum radar processing gain (equal to the bandwidth–time product $B{\cdot}T$) overcome the gain of the ESM even when the interceptor is at a relatively close distance. The aim of the LPD/LPI feature is that the ESM, despite its *"one way"* attenuation versus the *"two way"* of the radar, has to be able to detect the radar signal only at shorter ranges than the radar range.

Moreover, the LPD/LPI features are improved when the radar is working in Continuous Emission (CE) mode, which allows the radar emission to be more and more unpredictable thanks to a lower (than the pulse radar mode) peak power. Another relevant feature of CE radar is the lack of the *"pulse length"* signature in the waveform: the trailing and leading edges of radar pulses are one of the *"classical"* ESM/ELINT data.

A common way to improve the anti-interception performance of a radar set is to use the *"agility"* of the emission parameters (carrier frequency, pulse repetition interval, signal coding and so on) [5, 6]. In a CE-NR, it is possible to randomly vary (*time stagger*) the duration T and also (*agility*) $f_0 \pm \frac{B}{2}$. Limiting to the *time stagger*, if we set $T = d \cdot \frac{2R_{max}}{c}$, where d is a random variable with *uniform* law in the interval from 4 to 6 to guarantee an acceptable mismatching loss (less than 1 dB for $d = 5$), the detection will become much more difficult with a superiority of CE-NR over the conventional radar in terms of LPI and LPE.

1.3 | "Randomness" of NR waveforms and LPI features

A *"randomisation"* of the radar emission leads to the Continuous-Emission Noise Radar Technology (CE-NRT), where the whole radar emissions are pseudorandom waveforms, [7–9], with some intrinsic anti-intercept feature related to their *"amount of randomness"*, [10]. It is hard to quantify this *"randomness"*, as the Information Theory and the concept of Entropy do not seem to lead to advances beyond some basic theoretical evaluations, [11]. Of course, from the entropy point of view, the *most LPI* signals are the realisations of Gaussian noise occupying the maximum allowed frequency band. In this case, entropy is easy to comput being simply related to the flatness of the power density spectrum. This feature is quantified by the Spectral Flatness Measure, or SFM [12]. Unfortunately, in practice, these Gaussian signals have a rather high (around 10) PAPR (see Equation (1) in section 2), which does not fully exploit the transmitter power and does not maximise the signal-to-noise ratio (SNR). For a non-Gaussian process, which is the result of constrains of the amplitude for a *"low PAPR"* waveform, one should compute the *"reduction of entropy"* or *Negentropy* with respect to the Gaussian case [11].

Another element affecting the *amount of randomness* in NRT is the use of pseudo random number generators (PRNG's). The bare definition of a PRNG is *"a deterministic computational process that has one or more inputs called "seeds", and outputs a sequence of values that appears to be random according to specified statistical tests"* [13]. In other terms, the output of a PRNG *appears random to an external, well-defined observer*. This *black box* definition brings attention to the opponent trying to mimic "our own" signals and calls for a modelling of the interception process. However, we believe that the *"not really random"* behaviour of any PRNG, surely relevant in other applications such as cryptography, will not practically affect the LPI of a Noise Radar. In fact, there are substantial differences in these two domains: (i) when trying to break a crypto code, "every bit counts" and all bits are supposed to be error-free, while radar interception has to cope (not with bit streams but rather) with signal samples (with a given digital coding) unavoidably corrupted by noise and interference (mostly due to superimposed signals from many radar sources); and (ii) the repetition period of a suitable digital PRNG is much longer than a radar operation. The aforementioned periodicity problem is made immaterial by generation algorithms such as the *Mersenne Twister* [14], whose period is the huge $2^{19,937}-1$ for 32-bit integers. In practice, the period of the sequence is a minor problem with respect to the low statistical quality of some widely used PRNGs.

Finally, a flat power spectrum in the radar frequency band corresponds to relatively high range sidelobes at the matched filter output. Hence, both high *PAPR* and high sidelobes may be mitigated by *"tailoring"* the waveform. Clearly, both

compensations of the previous effects reduce the *uncertainty* of the signal thereby tending to impair its LPI.

Recent works in the literature show the use of the artificial intelligence (AI) in the waveform design to tailor the power spectrum. In Refs. [15–17], deep neural networks (DNN) are trained to design a phase-coded waveform with a power spectrum containing a low-power notch to support spectrum sharing.

The major advantages using a noise waveform are [18] (i) the inherent immunity from radio frequency and electromagnetic interference, (ii) the improved spectrum efficiency and, finally, (iii) protection against hostile jamming as well as being very difficult to detect.

Starting from the fact that finer range resolution in radar imaging requires high-bandwidth waveforms, that is, very fast analog-to-digital converters (ADCs), compressive sensing is a practical approach to lower sampling rates. In Ref. [19], noise signals are used as transmit waveforms to validate the feasibility of using compressive sensing for radar range imaging applications.

In a real environment, because of the presence of clutter and interferences from many other electromagnetic signals, the detection/interception/identification and localisation of a radar emitter by ESM/ELINT are *significant problems*. Typical approaches in a real-time identification of a pulse radar compare the characteristics of the pulse (synthesised in the Pulse Description Message, PDM [2] or Pulse Description Word, PDW) with the ESM *libraries*. Anyway, identification can be a very difficult task when (i) there are no records in an ESM library; (ii) there are overlaps of different radar parameters; (iii) the environment density quickly increases (e.g. because of Doppler radars transmitting hundreds of thousands of pulses per second); (iv) agility of the radar features (e.g., pulse repetition interval, carrier frequency and codes) is implemented; and (v) distortions and high noise levels lead to erroneous analyses.

1.4 | Analysis of LPI radar signals

The limitations in the detection/interception of radar signals, amplified to the wide deployment of radar systems with complex modulations (the most widely used term in ED is MOP: Modulation On Pulse), push research and development efforts to investigate novel extraction methods of radar parameters in comparison with the classical parameters (i.e. the radio frequency, the bandwidth, the pulse amplitude, the pulse width, the time of arrival and the direction of arrival).

In Time–Frequency (TF) analysis [20, 21], the Time–Frequency distribution (TFD) seems a powerful tool to deal with non-stationary signals as LPI signals. Many tools, based on TFD, have been developed to analyse the behaviour of non-stationary waveforms.

Historically, the classical work on Time/Frequency distribution dates back to 1932 (Wigner, [22]) and was initially motivated by the idea to evaluate a joint time/frequency distribution of the energy to study the problem of statistical equilibrium in quantum mechanics. Gabor [23] and Ville [24] further developed this approach by applying it to the communication signals by the Gabor transform and Wigner–Ville Distribution (WVD) using the *analytic signal*. In 1989, Cohen [25] generalised a wide class of TFD, introducing different kernel functions. Subsequently, Choi and Williams, using an *exponential* kernel function [26], improved the resolution and reduced the *cross terms* in comparison with the WVD. Details on TFD's are summarised in Appendix A.

The advent of fast and memory-efficient algorithms for computing the TFD [27] has favoured applications for the interception and identification of radar signals.

Generally, an automatic radar waveform recognition system, based on Time–Frequency analysis, is composed of four conceptual modules [28], as shown in Figure 1.

(1) *Tim–Frequency (TF) Processing*, that is, evaluation of the TFD and its 2D-image of the modulus.
(2) *Image Feature Extraction* that uses the 2D-image to extract the TF features [29].
(3) *Signal Feature Estimation*, obtained from the input signal to extract the main features: power spectral density, instantaneous frequency, bandwidth and so on [30, 31].
(4) *Classifier* for the classification of the victim radar signal.

A fifth block—*Off-line Training*—works off-line to train the classifier.

There is a wide variety of classifiers to improve the radar emitter recognition and identification [5]. Many proposed radar emitter recognition systems incorporate competitive learning, such as the Convolution Neural Networks (CNN) for their parallel architecture, fault tolerance and ability to handle incomplete radar information [32]. In Ref. [33], Wigner–Ville distribution (WVD) is employed in a CNN to classify incoming waveforms into Linear frequency modulation radar signals (LFM), single carrier radar signals (SCR), phase coded radar signals with three-element Barker code (PCR3), frequency coded radar signals with five-element Costas code and non-linear frequency modulation radar signals (NLFM). They employ time–frequency images as inputs to the network. In Ref. [34], the I–Q time series is employed for both CNN and LSTM (Long Short-Term Memory) and then a transfer learning framework is applied. Some methods use the wavelet packet transform (WPT) to extract the features and then a probabilistic support vector machines (SVM) to implement the radar emitter recognition [35–37]. To improve the performance of the signal extraction, *deep learning* uses multiple hidden layers perceptron to guarantee a more effective in the extraction of the signal, see for istance [38–44].

In principle, after transforming the TFD into a 2D-image, by suitable image processing algorithms, for example, *enhancements* of the TFD image, adaptive *binarisation* and *morphological* processing of the image [45], the shape of the TFD is a potential input to the identification and classification of radar signals.

This approach, for a Linear FM-CW radar signal, was applied in Refs. [46, 47], where the WVD and the Hough

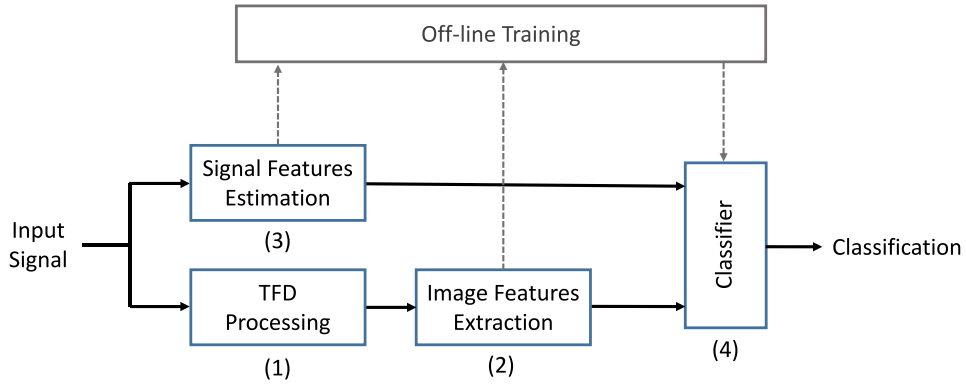

FIGURE 1 Automatic radar waveform recognition system.

transform (HT) were used to identify the parameters of the modulation. In Ref. [48], LFM radar signals are described by the PDW which assigns a label to each LFM pulse. By simulation, the authors showed that the filtering of cross-term interference in the TFD by suited kernel functions can degrade the performance of a Deep Learning LPI pulse classifier. In Ref. [49], a field-programmable gate array (FPGA) is used to design an embedded solution with low computational complexity for a Wigner–Hough transform to detect and extract the parameters of LFM-CW signals.

Recent literature is flooded by many other papers on the usage of various TFD analyses followed by Artificial Intelligence (AI) processing to classify radar signals in a limited (order of 10) number of classes. Comments on this approach are exposed in section 5 of the present paper, and no further references are added here.

The paper is organised as follows. Section 2 describes three different approaches to generate CE-NRT waveforms, and the related TFDs are compared. Section 3 introduces the detection of a radar source by a two antennas and correlator system as applied to intercept pseudorandom waveforms. Section 4 shows some considerations on the generation of Continuous Emission noise waveforms and the estimation of the bandwidth-duration parameters B and T. In section 5, we underline some limitations in the classification of radar signals using TFD. Section 6 reports final considerations.

2 | NOISE RADAR WAVEFORM GENERATION

In this section, we approach the pseudorandom waveform generation gradually. First, in section 2.1, the unpredictability of the signal is considered to be passing from deterministic to fully pseudorandom waveform. In section 2.2, two different methods (FMeth and COSPAR) to generate *"tailored"* pseudorandom waveforms are described.

The effectiveness of a radar waveform with a complex envelope $s(t)$ in terms of power (hence, of signal-to-noise ratio (SNR) at the output of the matched filter) is commonly measured by the PAPR as follows:

$$PAPR = \frac{\max_k |s[k]|^2}{\frac{1}{N}\sum_{k=1}^{N} |s[k]|^2} \tag{1}$$

where $s[k]$, with $k = 1, 2,\ldots,N$, are the samples of the signal (typically, at the Nyquist rate).

The $PAPR$ assumes values in the range $[1, PAPR_{Max}]$ where $PAPR_{Max}$ (in the following called *"natural" PAPR*) for Gaussian statistics is of the order of 10 or slightly more [8]. The loss of SNR is related to the $PAPR$:

$$Loss = 10 \cdot log_{10}(PAPR) \tag{2}$$

Hence, there is no loss for $PAPR = 1$ and about 10 dB for *natural PAPR*.

2.1 | A phase noise waveform generator based on Non-Linear Frequency Modulation

The general expression of the complex envelope of a modulated deterministic waveform of bandwidth B and duration T (compression ratio $BT = B \cdot T$) is

$$s_{det}(t) = a(t) \cdot e^{j\phi_{PM}(t)} \; -\frac{T}{2} \leq t \leq +\frac{T}{2} \tag{3}$$

where $a(t)$ and $\phi_{PM}(t)$ are the Amplitude Modulation (AM) and the phase Modulation (PM), respectively. The derivative of $\phi_{PM}(t)$, in radians, is the frequency modulation function $\phi'_{PM}(t)$ or instantaneous frequency. A suitable choice of $a(t)$ (amplitude weigthing function) and $\phi'_{PM}(t)$, that is, a Non-Linear Frequency Modulation (NLFM) theoretically may control the peak sidelobe levels (PSL) of the signal reaching low PSL. In the following, we consider two NLFM signals to generate noise waveforms.

- First, a Hybrid-NLFM signal where $a(t)$ is evaluated by applying the *stationary phase principle*:

$$a(t) \cong \sqrt{\frac{1}{2\pi}\left|S\left[\phi'_{PM}(t)\right]\right|^2 \cdot \left|\phi''_{PM}(t)\right|}$$

with $S\left[\phi'_{PM}(t)\right]$ the spectrum of $s_{det}(t)$ at the instantaneous frequency $\phi'_{PM}(t)$ and $\phi''_{PM}(t)$ the second derivative of $\phi_{PM}(t)$. The law of the instantaneous frequency $\phi'_{PM}(t)$ is supposed a weighted sum of a Non Linear-tangent FM term and a LFM one (this justifies the name *hybrid*), [50]:

$$\phi'_{PM}(t) = \pi B\left\{\alpha \frac{1}{tg(\gamma)} tg\left(\frac{2\gamma B}{T}\right) + (1-\alpha)\frac{2t}{T}\right\} \; t \in \left[-\frac{T}{2}, +\frac{T}{2}\right]$$

where $\alpha \in (0,1)$ is the relative weight, B is the sweep frequency, γ is the Non-Linear-tangent FM rate. The weighting coefficients (α, γ) have been optimised (for a signal with a Gaussian spectrum) maximising the transmission efficiency in comparison with the rectangular amplitude ($PAPR = 1$). The related loss results in 0.58 dB only, corresponding to $PAPR \cong 1.14$. Details on Hybrid-Non-Linear-FM (HNLFM) waveforms are reported in Ref. [50]. These types of signals can reach very low PSL (<−70 dB) also for $BT = 128$ and 256, maintaining the $PAPR$ close to the unity.

- Second, the well-known Hamming NLFM signal with a uniform amplitude and spectrum following a square root of raised cosine-squared.

Multiplying the deterministic signal $s_{det}(t)$, Equation (3), with $e^{jk\cdot\varphi(t)}$, where $\varphi(t)$ is a pseudorandom process (that is, for each t, $\varphi(t)$ is a *Uniform-distributed* random variable in $[0, 2\pi]$) and $k \in [0, 1]$ is a parameter), we define the *phase-noise* waveform:

$$s(t) = s_{det}(t) \cdot e^{jk\cdot\varphi(t)} \tag{4}$$

In Ref. [51] this type of signal is named as Advanced Pulse Compression Noise (APCN).

For $k = 0, 0.25, 0.5$ and 1.0, Figure 2 shows the related Pseudo-Smoothed Wigner–Ville Distribution (PSWVD) of a HNLFM realisation when $BT = 5000$. For $k = 0$ (deterministic HNLFM signal) the PSL is reduced to a very low value (less than −100 dB) as shown in Figure 3a. However, introducing the phase noise (k>0), the performance is downgraded (see Figures 3b,c,d). Particularly, for $k = 0.25$ the PSL is around −37 dB, for $k = 0.5$ the PSL is −32 dB and for $k = 1.0$ the PSL is around −31 dB.

Considering a Hamming NLFM signal ($PSL \cong -42.8$ dB) to generate the phase noise waveform (setting the previous BT = 5000), Figure 4a shows the PSWVD for $k = 0$ which is easily distinguishable from Figure 2a, but, when the phase noise is introduced into the signals, $k = 0.25$, 0.5. 1.0, the two waveforms gradually become less distinguishable (compare Figures 2b,c with Figures 4b,c), becoming indistinguishable for $k = 1.0$ (see Figures 2d and 4d) although the SNR is infinity. This indistinguishable waveform is very important for the LPI feature.

We conclude the section understanding that in literature, there are approaches similar to APCN to generate phase noise signals, [52].

2.2 | Tailored waveforms for NRT

The above-referenced APCN waveforms design does not include the PAPR and PSL control; in order to achieve these important features, two approaches (FMeth and COSPAR generators) are presented and analysed in the following. Other methods, not described here, are shown in literature [15–17].

2.2.1 | FMeth pseudorandom generator

FMeth (filtering method) is a procedure to generate pseudorandom waveforms starting from the generation of white Gaussian complex sequences with a *uniform* spectrum, see the block diagram of Figure 5. At the output of the spectral shaping (Fast Convolution Generator, FCG, by filtering inside the selected band B), the pseudorandom signal $g(t)$ shows a *natural PAPR* (around 10 or greater), with an assigned spectrum (e.g. Blackman–Nuttall, Hamming, etc.), whose inverse Fourier transform (i.e. the autocorrelation function) shows better PSL with respect to the one derived from the *uniform* spectrum (13 dB only). However, high *PAPRs* result, causing a low power efficiency. To improve the transmitted mean power, the *PAPR* can be reduced (typically to 1.5–2.0) by the *PAPR Set by Alternating Projection* block (middle of Figure 5), maintaining an acceptable SNR (loss around 2–3 dB). The idea behind the *alternating projection algorithm* is to search for a point of intersection between the *spectral* constraint and a *structural* constraint. In our case, the spectral constraint is determined by the spectral occupancy of the generated waveform, and the structural constraint is the desired PAPR. The output from the *PAPR Control*, $g_1(t)$, has the assigned *PAPR* with non-Gaussian distribution of the in-phase (I) and in-quadrature (Q) components. A further reduction of the PSL near the mainlobe of the autocorrelation function of $g_1(t)$ (useful to attenuate the harmful effect of the antenna leakage and the near clutter) can be achieved by an approach, here named FMeth, based on the concept of *"inverse filtering"*, well known in literature [53], whose main operational steps, as shown in Figure 5, are as follows:

(i) Evaluation of the autocorrelation $R(\tau)$ of $g_n(t)$, at the initial step $n = 1$.
(ii) Definition of the desired autocorrelation: $\tilde{R}(\tau) = R(\tau) \cdot q(\tau)$ in order to suppress the range sidelobes inside the time interval $\Omega = [-\tau_2 < \tau < -\tau_1] \bigcup [\tau_1 < \tau < \tau_2]$, where the function $q(\tau)$ is $q(\tau) = \begin{cases} 0 \; \tau \in \Omega \\ 1 \; elsewhere \end{cases}$.

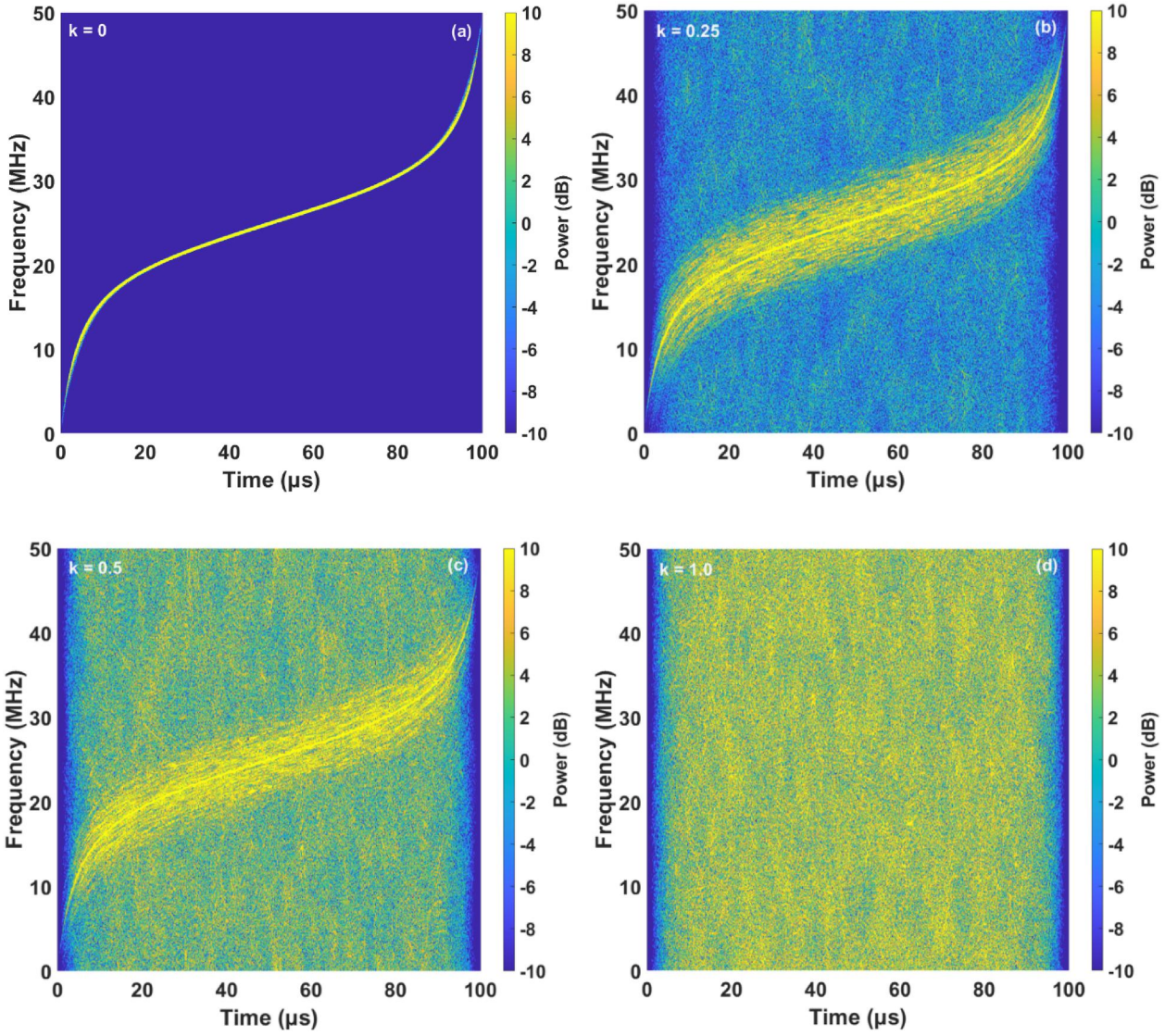

FIGURE 2 Pseudo-Smoothed Wigner–Ville Distribution (PSWVD) of an Advanced Pulse Compression Noise (APCN) with Hybrid-Non-Linear-FM (HNLFM), BT = 5000, varying the rate: (a) $k = 0$, (b) $k = 0.25$; (c) $k = 0.5$; (d) $k = 1$. Receiver noise: absent.

(iii) Estimation by FFT of the Fourier transform $G(f)$ of $g_1(t)$ and of the spectrum $\tilde{S}(f)=\mathscr{F}\left[\tilde{R}(\tau)\right]$, where $\mathscr{F}[\cdot]$ denotes the Fourier transform.
(iv) Evaluation of the frequency response: $H(f)=\frac{\sqrt{\tilde{S}(f)}}{|G(f)|}$.
(v) Generation of the random signal $\hat{g}_n(t)$, with attenuated sidelobes of the autocorrelation inside Ω, by $\hat{g}_n(t)=\mathscr{F}^{-1}\{H(f)\cdot G(f)\}$.

Due to the detrimental effects related to the use of the FFT, that is, the folding of the spectral components of $q(t)$ into $(-B/2, +B/2)$, the output $\hat{g}_n(t)$ has to be iteratively processed by the FMeth algorithm for a suitable number of times ($n = 1, 2,\ldots,n_{iter}$) to improve the sidelobes suppression until the requirements are satisfied.

We underline that a possibly large number of iterations is not a practical problem for this this procedure to be designed for an offline preparation of a large number of transmit signals. A more detailed description of the FMeth noise waveform generator is available in Refs. [8, 9].

2.2.2 | COSPAR generator

COSPAR is the acronym of COmbined Spectral-shaping and Peak-to-Average power ratio Reduction and denotes a waveform generator that uses a *uniform* random variable θ in $(0, 2\pi)$ to generate the samples of a pseudorandom signal. This method appears to be an easier way to create a tailored noise waveform. Unlike FMeth, the COSPAR generator has no iterations for sidelobes control. Figure 6 shows the related block diagram [54].

First, the power spectrum $S(f)$ is selected, choosing among suited frequency windows (i.e. Taylor, Hamming, Blackman–

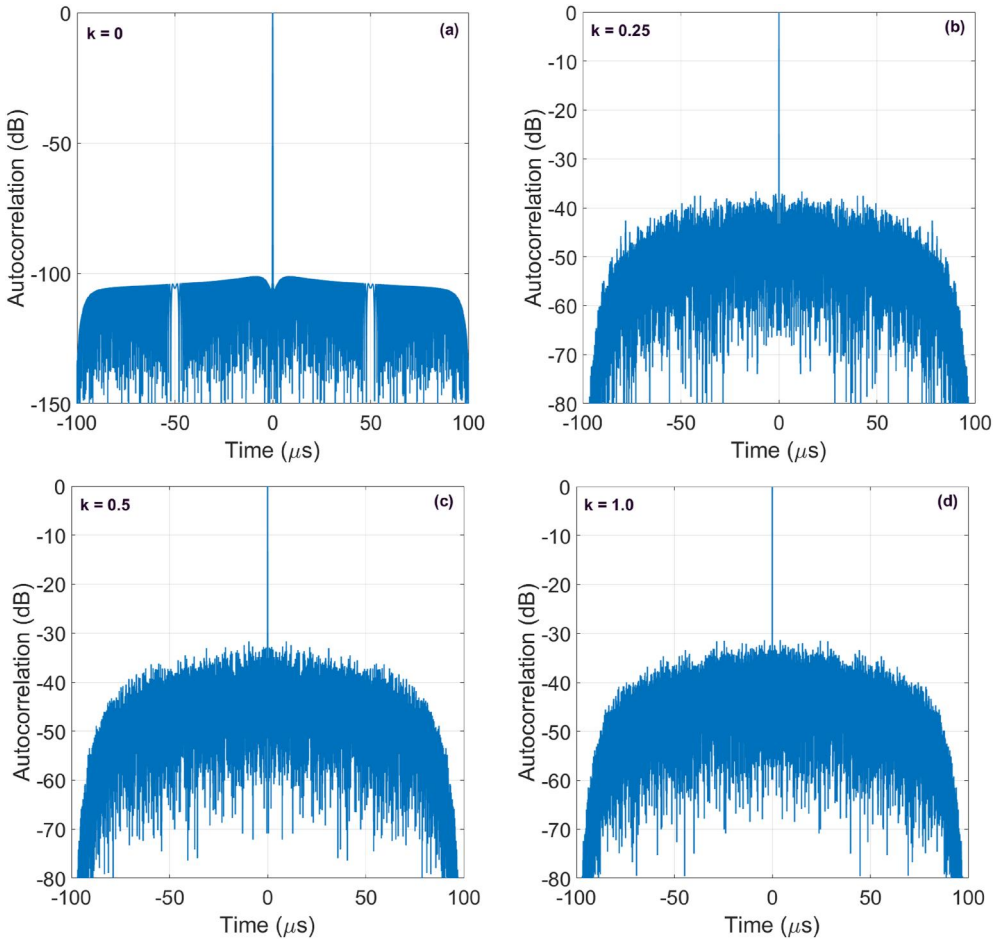

FIGURE 3 Normalised Autocorrelation of an Advanced Pulse Compression Noise (APCN) with Hybrid-Non-Linear-FM (HNLFM), varying the rate: (a) $k = 0$, (b) $k = 0.25$; (c) $k = 0.5$; (d) $k = 1$. BT = 5000. Receiver noise: absent.

Nuttall, etc.). Then, the root square of $S(f)$ is computed to define the amplitude of the spectrum of the pseudorandom waveform, that is, $G(f) = \sqrt{S(f)}$. The randomness of the signal is introduced in the phase of the spectrum by a random number generator of a *uniform* random phase $\theta \in (0, 2\pi)$. Finally, the complex spectrum $Z(f) = G(f) \cdot \exp\{j\theta\}$ is obtained. By Inverse-Fast Fourier Transform (*IFFT*), we compute the sequence $z(n)$ in the time domain. Because the length of $z(f)$ is much greater than one, applying the Central Limit theorem to $IFFT\{Z(f)\}$, this transformation makes the components I and Q Gaussian-distributed in the time domain. The control of the *PAPR* is implemented using the *PAPR reduction algorithm* as described in Ref. [54].

We underlay that, using this method, all generated sequences (although pseudorandom) have the same (deterministic) power spectrum and autocorrelation function. Figures 7a and 8a show, for *natural PAPR* and *PAPR* = 1.5, the spectrum of a single realisation ($M = 1$) of a pseudorandom signal obtained by applying the FMeth (blue line) and the COSPAR (red line) generator, starting from the same Blackman–Nuttall frequency window with $BT = 5000$.

2.2.3 | Interception of FMeth and COSPAR waveforms

An alternative interception method (aided by the spectral analysis) for waveforms of the above-referenced type uses the following steps. (i) Acquisition of M realisations of the waveforms. (ii) Computation, via FFT, of the spectrum. (iii) Computation of the squared modulus of the spectrum. and (iv) Average of M squared moduli (for each frequency). The results, with $M = 100$, are shown in Figures 7b and 8b. Note that the COSPAR generator is able to produce the same power spectral density for different PAPRs, [54].

In Figure 9 (9a and 9b for natural PAPR, 9c and 9days for PAPR = 1.5), the Pseudo-Smoothed Wigner–Ville distributions of a realisation are shown to compare FMeth and COSPAR ($B = 50$ MHz, $T = 100$ μs, Blackman–Nuttall frequency window). If we considered another pair of realisations, we would observe similar images but different from the previous ones. Hence, the identification of features, which is able to automatically recognise by time–frequency distribution waveforms, appears to be nearly impossible.

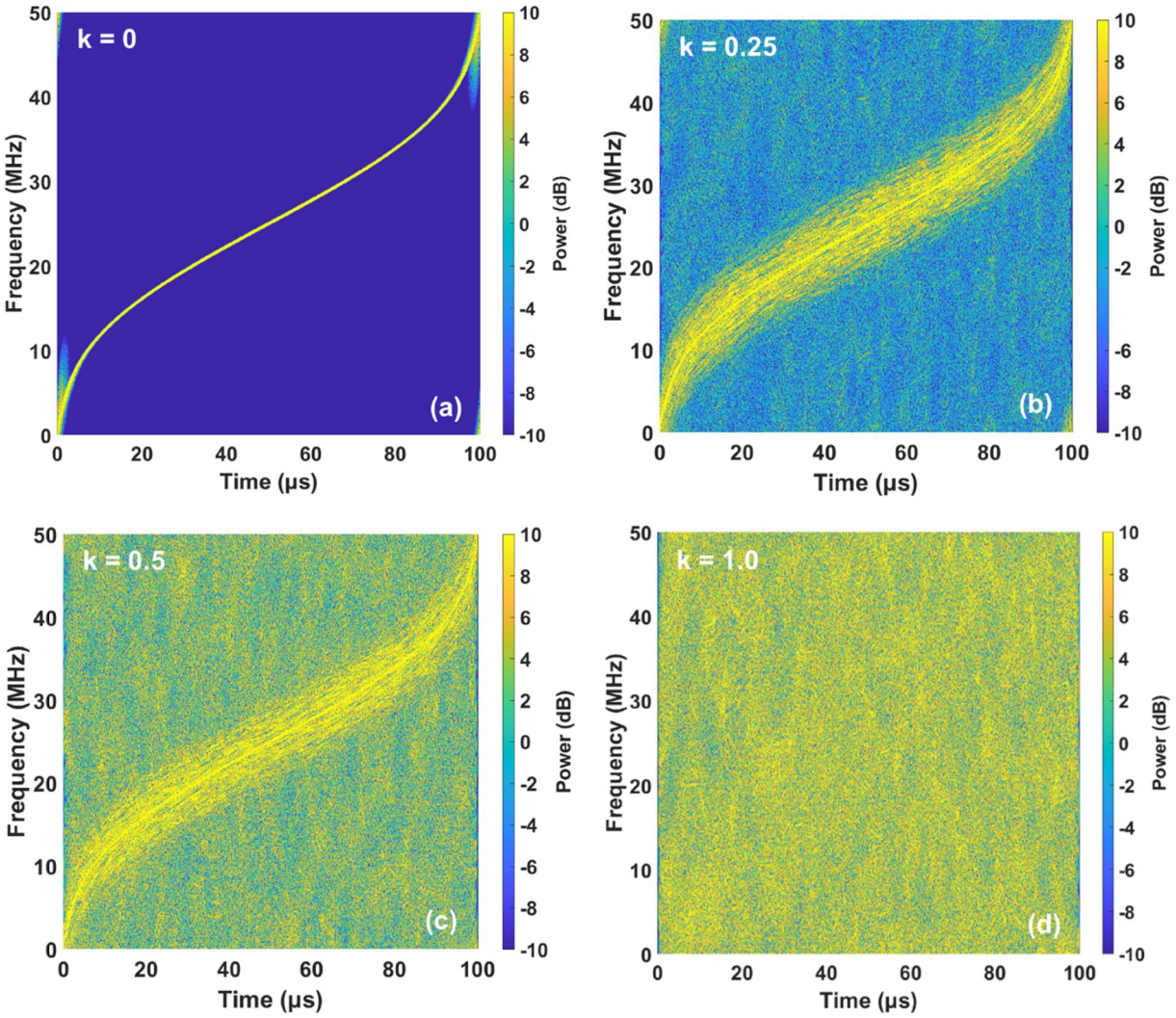

FIGURE 4 Pseudo-Smoothed Wigner–Ville Distribution (PSWVD) of an Advanced Pulse Compression Noise (APCN) with Hamming Non-Linear Frequency Modulation (NLFM), BT = 5000, varying the rate: (a) $k = 0$, (b) $k = 0.25$, (c) $k = 0.5$, (d) $k = 1.0$. Receiver noise: absent.

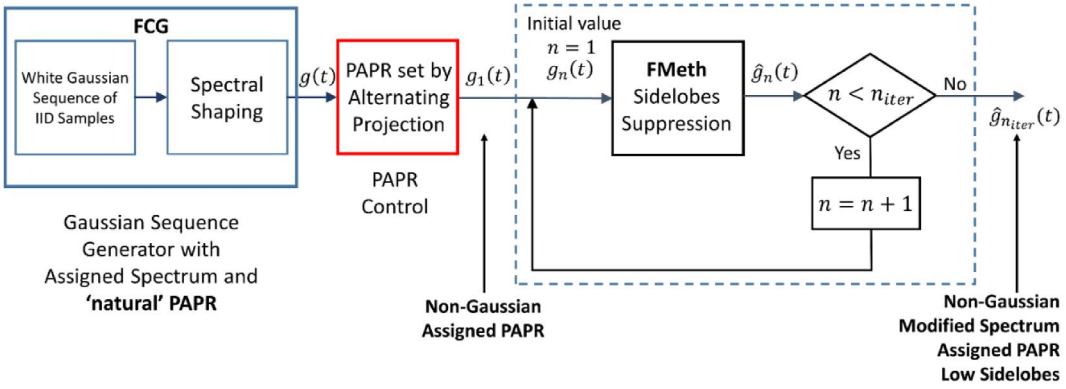

FIGURE 5 FMeth waveform generator.

An approach similar to COSPAR is described in Ref. [55], where the design of pseudo-random optimised FMCW waveforms is proposed using spectral shaping optimisation. The waveform has shown good spectral containment and range sidelobes below −75 dB. In Refs [56, 57], spectral notches were incorporated in the spectral shaping optimisation to favour the spectrum sharing permitting to reject narrowband interferences.

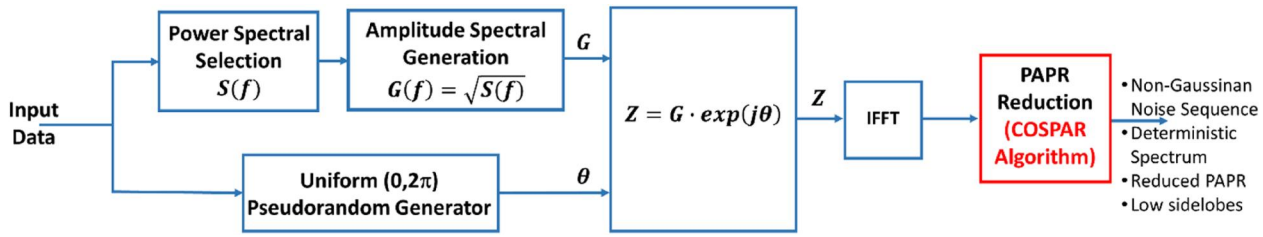

FIGURE 6 COmbined Spectral-shaping and Peak-to-Average power ratio Reduction (COSPAR) waveform generator.

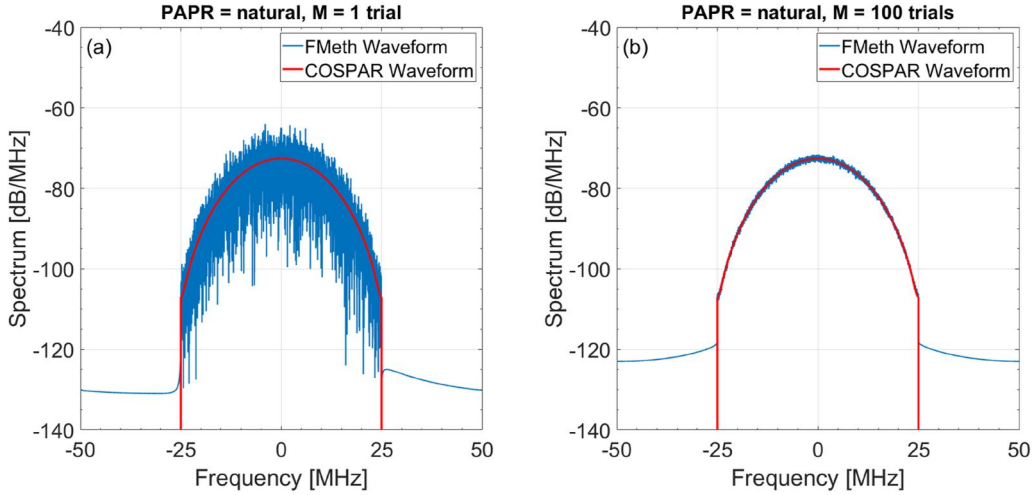

FIGURE 7 Estimated spectrum of FMeth and COSPAR waveforms, $B = 50$ MHz, $T = 100$ μs, Peak-to-Average Power Ratio (PAPR) = natural. (a) $M = 1$ realisation; (b) $M = 100$ realisations. Receiver noise: absent.

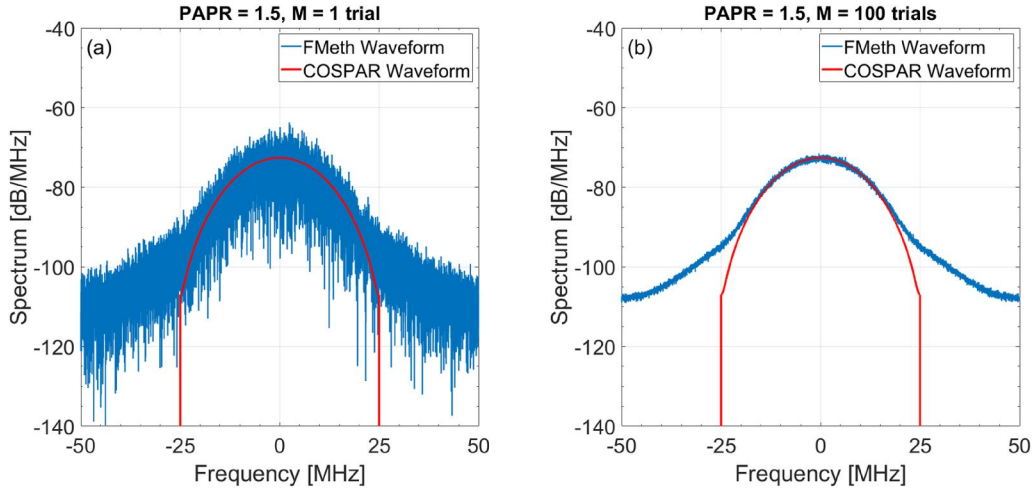

FIGURE 8 Estimated spectrum of FMeth and COSPAR waveforms, $B = 50$ MHz, $T = 100$ μs, Peak-to-Average Power Ratio (PAPR) = 1.5. (a) $M = 1$ realisation; (b) $M = 100$ realisations. Receiver noise: absent.

Summing up, the APCN generator has been useful to describe the transition from a deterministic signal to a more and more random signal. For the two generators, FMeth and COSPAR, the latter is simpler to implement; however, its main limitation with respect to FMeth is that all generated waveforms have the same spectrum, that is, they are more easily classified.

3 | DETECTION OF A RADAR SOURCE

The detection of a radar signal by ESM or ELINT systems differs from the conventional radar detection, where the transmitted signal is known and the matched filtering grants the maximum gain in signal-to-noise ratio (*SNR*).

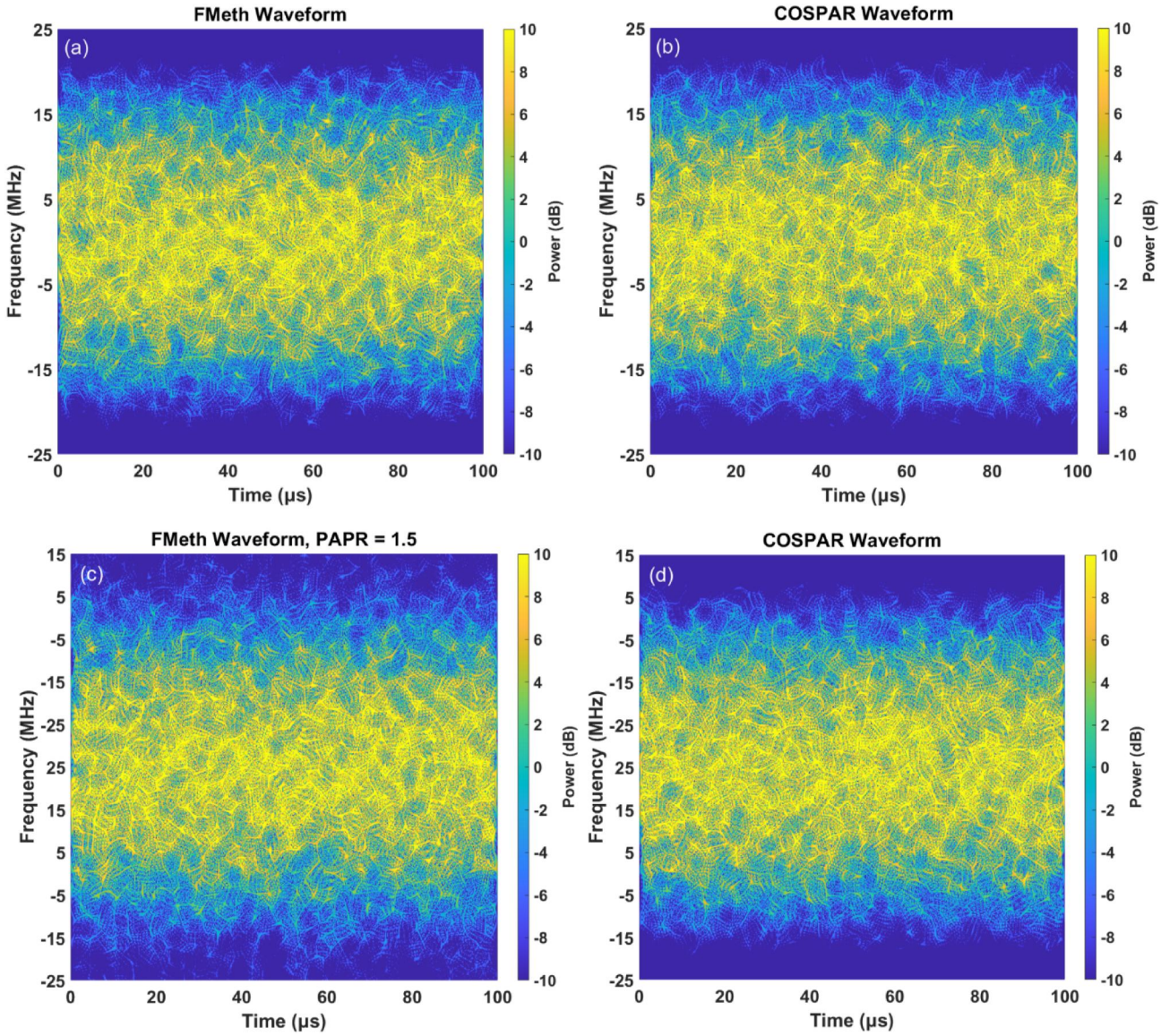

FIGURE 9 PSWV Distribution of a single realisation. (a) FMeth waveform, natural Peak-to-Average Power Ratio (PAPR); (b) COSPAR waveform, natural PAPR; (c) FMeth waveform, PAPR = 1.5; (d) COSPAR waveform, PAPR = 1.5. Receiver noise: absent.

The most popular detector to intercept a spread spectrum signal is the *energy detector* (ED), which ignores the structure of the signal and simply compares its energy with a noise threshold. To intercept coherent signals, a possible improvement is to use a *multiple antenna receiver*. In the following, we consider the *two antennas and correlator* (2A&C) receiver [58–60] as shown in Figure 10. In Ref. [4], the statistical features of the 2A&C are shown for *deterministic* radar signals. The extension to *pseudorandom* signals is described in Refs. [61–63] and synthesised in Appendix B. The basic features are resumed in the following.

The noise contribution is uncorrelated between the two receivers; hence, the computed correlation is only due to the signal of interest (SOI) at the input of both receivers. By fast ADCs (Analog-to-Digital Converters) with a few GS/s of the sampling rate and FPGA (Field Programmable Gate Arrays), the processing achieves wideband sampling and digital filtering (each pass-band filter intercepts the signal in the sub-band), whose outputs $(\boldsymbol{y}_1,\boldsymbol{y}_2)$ represent the complex envelope of the corresponding signal from the intercepted sub-band.

For each sub-band, the cross-correlation is computed between $\boldsymbol{y}_1$ and $\boldsymbol{y}_2$, which represent the samples (at the Nyquist rate) of the sum of $\boldsymbol{s}$ (SOI if present) with the receiver noise $\boldsymbol{n}_1$ and $\boldsymbol{n}_2$ respectively.

In Appendix B, for pseudorandom signals, the relationship between the input/output *SNR* and the probability of detection P_D (for the assigned probability of a false alarm, P_{FA}) is shown. The SNR_0 at the output versus the SNR_i at the input to the 2A&C is described by Equations (5a) and (5b) for deterministic and pseudorandom signals respectively, where the

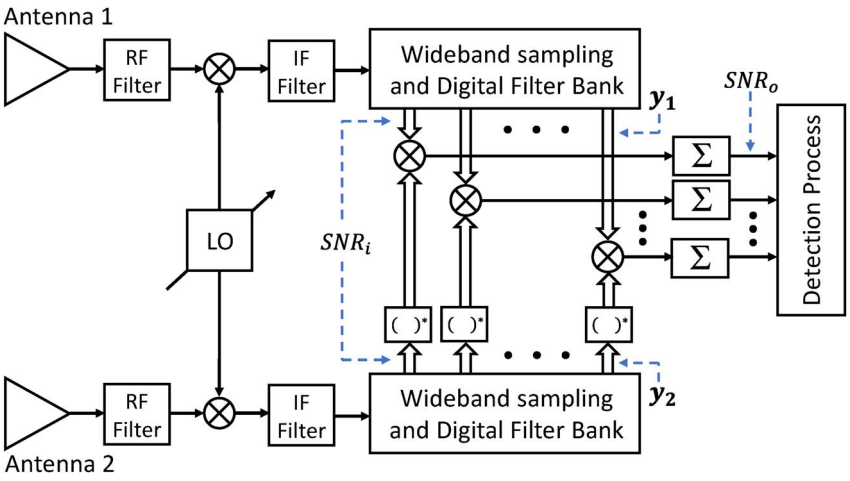

FIGURE 10 Two antennas and correlator system (2A&C). $()^*$ defines the conjugate operation. The vectors $\boldsymbol{y}_1$ and $\boldsymbol{y}_2$ denote the generic output from each filter (the filter indexes are omitted).

correlation time is assumed to be equal to the time duration of the signal T and the bandwidth B of the signal is supposed equal to the bandwidth of the receivers.

$$SNR_0 = BT\frac{SNR_i^2}{1+2{\cdot}SNR_i}\,(\text{deterministic}) \tag{5a}$$

$$SNR_0 = BT\frac{SNR_i^2}{1+2\cdot SNR_i+2\cdot SNR_i^2}\,(\text{random}) \tag{5b}$$

Figure 11 shows Equations (5a) and (5b) for BT equal to 10^2 (red), 10^3 (blue) and 10^4 (green). Similar results of Figure 11 are shown in Ref. [64].

Setting the probability of a false alarm P_{FA}, the probability of detection P_D can be written for both deterministic and pseudorandom signals as (see Appendix B) follows:

$$P_D = 1-F_{\chi_2^2}\left\{x=\frac{\eta}{\beta};\ \lambda=2\cdot SNR_0\right\} \tag{6}$$

where $\beta = 1+2\cdot SNR_i+2\cdot SNR_i^2$ for pseudorandom signals and $\beta = 1+2\cdot SNR_i$ for deterministic signals. The decision threshold is $\eta = -2\cdot ln\,(P_{FA})$ and the function $F_{\chi_2^2}(x;\lambda)$ denotes the cumulative distribution function of a *non-central chi-square* random variable with 2 degrees of freedom and *non-centrality parameter* λ.

From Figure 11, when $SNR_i \geq -5$ dB, the SNR_0 is even greater than 15 dB for $BT \geq 1000$ and both types of signals (pseudorandom and deterministic); hence, the probability of detection is close to *one* (see Figure 12, continuous lines, i.e. Equation (6), and diamonds for the computer simulation of FMeth signals). When $SNR_i < -5$ dB, the SNR_0 is approximated by $2\cdot SNR_i\,(dB) + G_{int}\,(dB)$ and there is no substantial difference between the two cases (the high level of noise no longer allows to distinguish between a random signal and a deterministic one). Summing up for a 2A&C receiver, a desired $P_D \geq 0.9$ is generally guaranteed for SNR_i greater than -13.4 dB ($BT = 10^4$), -8.3 dB ($BT = 10^3$) and -3.0 dB ($BT = 10^2$).

For comparison, Figure 12 shows the curves of P_D which is derived using the energy detector (ED); dashed lines are referred to the theoretical evaluation shown in Ref. [4], while circles are the estimated values by a computer simulation of FMeth pseudorandom signals. The improvement obtained by the 2A&C detector, versus ED, is around 1.5 dB for $P_D \geq 0.9$ (it is true also for deterministic signals).

The simulation data shown in Figures 11 and 12 are estimated using the FMeth generator (see Section 2.2.1) with a Blackman–Nuttall spectrum, $B = 50$ Mhz, *natural PAPR* (values around 10), without sidelobes suppression, with a signal duration of 100 μs.

The probability P_D is estimated by the relative frequency: $\hat{P}_D = \frac{n_{threshold}}{N_{trials}}$ (Maximum-Likelihood unbiased estimator) where N_{trials} is the number of trials and $n_{threshold}$ is the number of hits that overcome the threshold η for an assigned probability of false alarm P_{FA}, see Equation (B.8) in Appendix B. For a large number of trials, after the estimation of $\hat{P}_D$, its standard deviation can be approximated as $\hat{\sigma} \cong \sqrt{\frac{\hat{P}_D(1-\hat{P}_D)}{N_{trials}}}$. With $\hat{P}_D$=0.9 and $N_{trials} = 1000$, the standard deviation is $\hat{\sigma} \cong 0.01$.

For a 2A&C receiver, Figure 13 shows the estimates of $\hat{P}_D$ with $N_{trials} = 1000$ varying the SNR_i (dB) and the corresponding error bars ($\pm 2\hat{\sigma}$), same conditions as above.

Now, with $BT = 1000$, we verify by simulation that results from Equation (5b) are practically independent of (a) the pseudo-random waveform generator used, (b) the *PAPR* and (c) the spectrum used as input to the waveform generator.

Figure 14 compares the probability of detection of FMeth and COSPAR waveforms obtained with the same starting spectrum (Blackman–Nuttall) for high (*natural*) *PAPR* and low *PAPR* (=2). In Figure 15, for FMeth waveforms, the spectrum is varied from Hamming to Uniform.

We observe that the curves of P_D (even if related to a single realisation for each estimated probability P_D) are very similar to each other. This is due to the fact that, for very low SNR_i (negative values in dB), the receiver noise in some way masks the different settings with which the pseudorandom

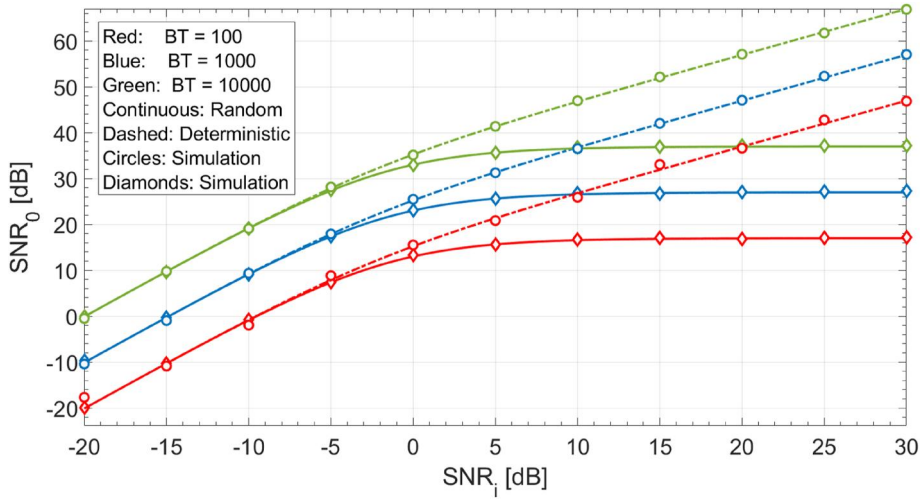

FIGURE 11 SNR_o versus SNR_i for 2A&C receiver. Dashed line: deterministic signals, Equation (1a). Continuous line: pseudo-random signals, Equation (1b). Circles and diamonds correspond to computer simulations on 1000 trials of FMeth pseudorandom signals. BT is equal to 10^2 (red), 10^3 (blue) and 10^4 (green).

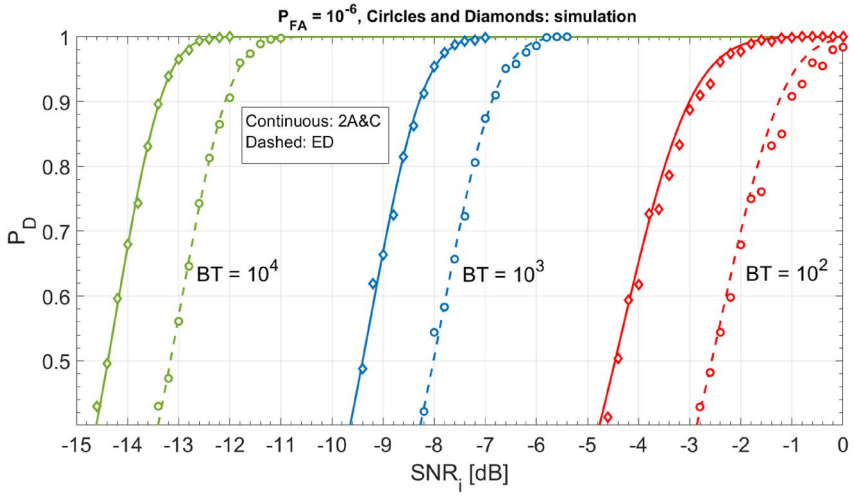

FIGURE 12 Probability of detection P_D versus SNR_i, Equation (6), for $P_{FA} = 10^{-6}$. Continuous line: 2A&C receiver. Dashed line: Energy Detector (ED) receiver. Diamonds and circles show the results of computer simulation, 1000 trials of FMeth signals. BT is equal to 10^2, 10^3 and 10^4.

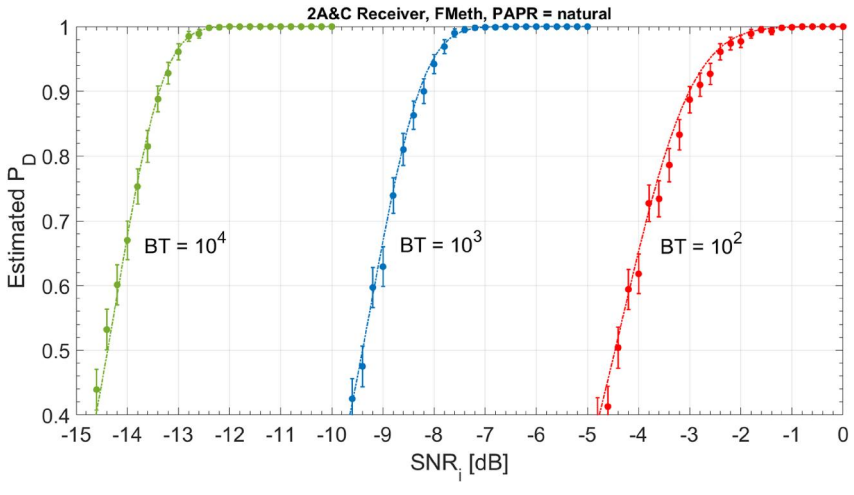

FIGURE 13 Estimated probability of detection (P_D) versus SNR_i [dB]. PAPR = natural with Blackman–Nuttall spectrum. FMeth generator. Simulation on $N_{trials} = 1000$. Error bar: $\pm 2\hat{\sigma} \cong \pm 2\sqrt{\frac{\hat{P}_D(1-\hat{P}_D)}{N_{trials}}}$.

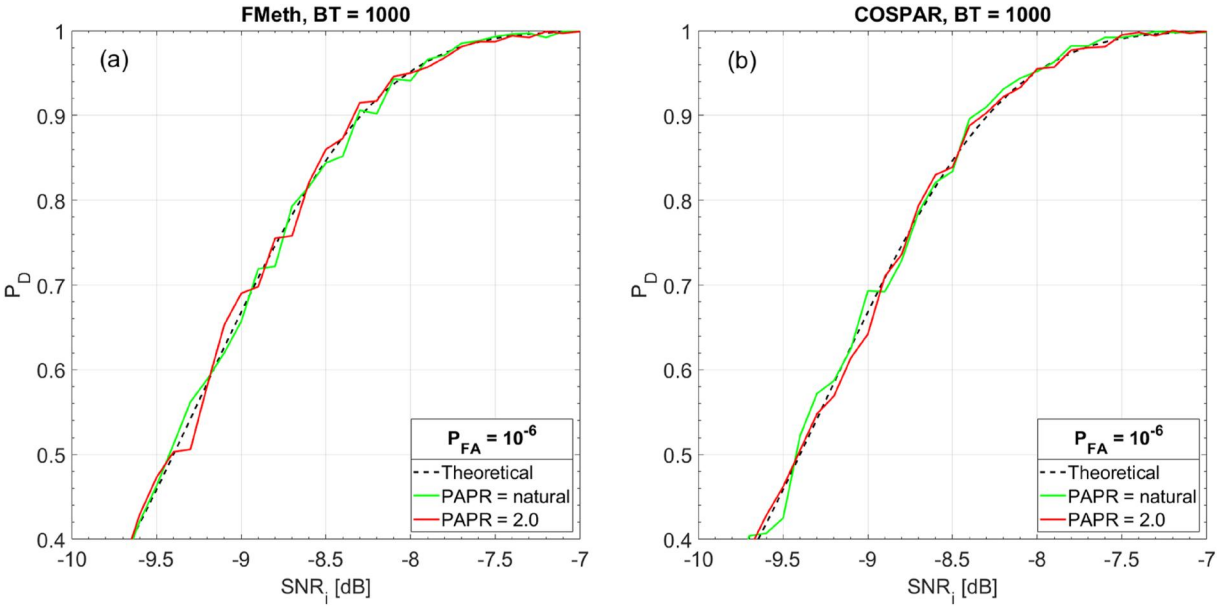

FIGURE 14 Estimated probability of detection (P_D) versus SNR_i [dB] for $BT = 1000$, PAPR = natural (green line) and PAPR = 2.0 (red line) with Blackman–Nuttall spectrum. (a) FMeth generator. (b) COSPAR generator. Simulation with 1000 trials.

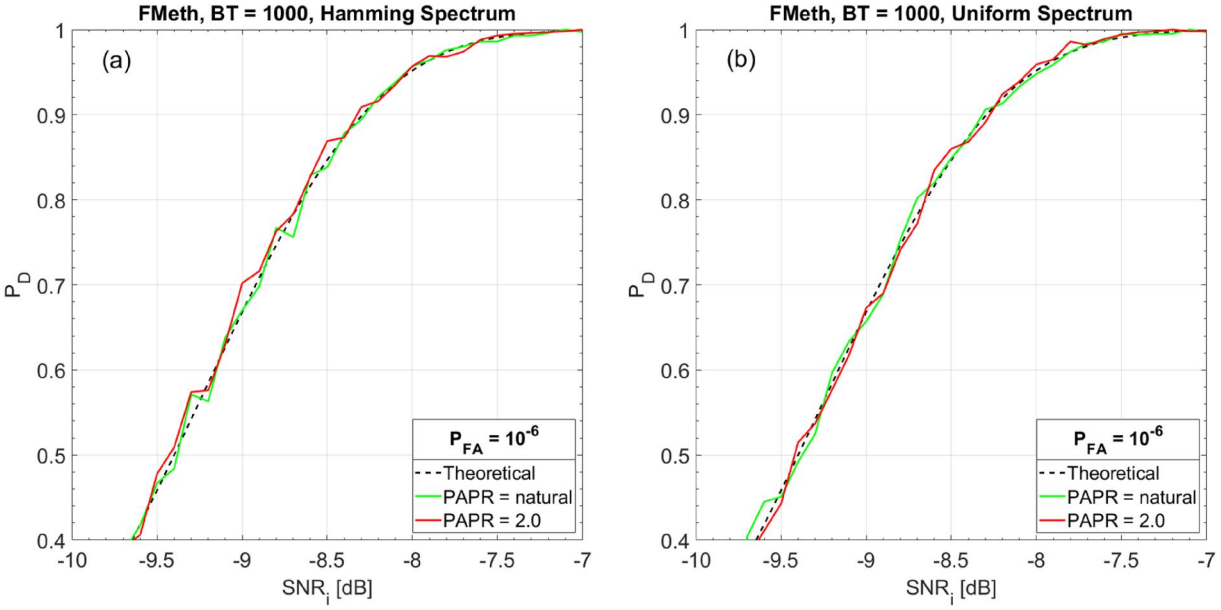

FIGURE 15 Estimated probability of detection (P_D) versus SNR_i [dB] for the FMeth generator, $BT = 1000$. PAPR = natural (green line) and PAPR = 2.0 (red line). (a) Hamming spectrum. (b) Uniform spectrum. Simulation with 1000 trials.

waveforms are generated (i.e. the type of the generator, the *PAPR* and the spectrum).

These results show that the detection of a pseudorandom signal by a two antenna receivers has similar performance to the one of a deterministic signal in the most critical cases, that is, when the SNR is low, irrespective of the waveform generation method.

These results apply to an ideal detection process exploiting the knowledge of the signal frequency band and duration, that is, of the central frequency f_0, the band B and the duration T of the modulation. In a real situation, estimating these parameters for a CE-NR of the opponent is not an easy task, especially concerning T. Some key aspects are discussed in the following.

4 | PARAMETERS ESTIMATION OF CE NOISE RADAR

As the generation of long duration waveforms for noise radar applications is not convenient, the practical solution is to generate, see section 2, contiguous independent signals $g_i(t)$ with bandwidth B and duration T_i, as shown in Figure 16a,

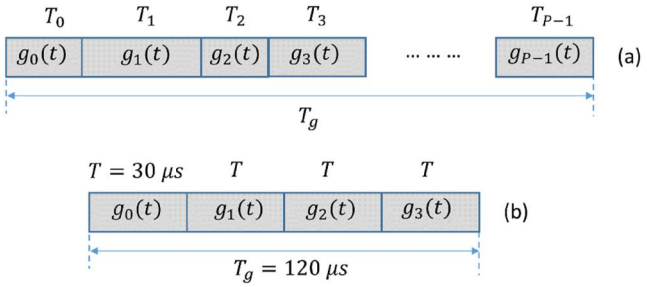

FIGURE 16 (a) Generation of the noise waveform for a CE noise radar with time stagger. (b) The examined case, no time stagger, $T = 30$ μs, $p = 4$.

where P is an integer generally much greater than one. The duration T_i is of the order of tens or hundreds microseconds, and it can be varied (time staggering) from $g_i(t)$ to $g_{i+1}(t)$, while the total time–length T_g is generally equal to the Coherent Processing Interval (CPI), typically of the order of some milliseconds. These parameters depend on the maximum instrumented range and the maximum Doppler frequency, see section 6.3 of [9, 65]. Their effects (as well as the effect of "staggering") on maximum instrumented range and Doppler measurement are somewhat similar to those of the classical Moving Target Detector (MTD), [66]. In Ref. [67] a novel optimal algorithm, named Range Filter Bank (RFB) is described with the aim to compute the ambiguity function in the delay and Doppler interval of interest, avoiding any unnecessary processing load.

The time-intervals T_i are very likely unknown to the enemy in both position and duration, who has to estimate them analysing the intercepted signal. A preliminary analysis in Refs. [62, 63] showed, for FMeth noise signals, that the bandwidth estimation may be used to evaluate T_i only when the side lobe suppression (SLS) function is applied (see section 2.2.1) and when there is a large enough (at least 5 dB or 10 dB) SNR with natural PAPR. This is easily understood when considering that the weighting of the power spectrum is necessary to reduce the level of the sidelobes of the autocorrelation function. In practice, the SLS function generates a lack of continuity between $g_i(t)$ and $g_{i+1}(t)$.

As an example (see Figure 16b for the construction of the noise waveforms), a rapid increase/decrease of the harmonic components is visible in the PSWVD (Figure 17a) for the FMeth signal with $B = 50$ MHz, SNR = 40 dB, $T_i = 30$ μs, $p = 4$ and PAPR = 8.8. In Figure 17b, the PAPR is reduced to 2.0, and the lacks of continuity disappear. This is due to the spectral widening effect of the non-linearity inherent to the PAPR reduction. Details of the analysis are as follows.

Denoting $P(t,f)$ the time/frequency distribution, the instantaneous bandwidth $BW(t)$ of the signal is estimated as the square root of the second central spectral moment [30, 31]:

$$BW(t) = \sqrt{\frac{\int_0^\infty [f - f_{inst}(t)]^2 \cdot P(t,f)\, df}{\int_0^\infty P(t,f)\, df}} \tag{7}$$

where $f_{inst}(t)$ is the instantaneous frequency, estimated as

$$f_{inst}(t) = \frac{\int_0^\infty f \cdot P(t,f)\, df}{\int_0^\infty P(t,f)\, df} \tag{8}$$

Figure 17c shows the estimated instantaneous bandwidth using Equations (7) and (8) with $P(t,f)$ the Pseudo-Smoothed Wigner–Ville Distribution (PSWVD). For PAPR = 8.8 (blue line), the peaks at the time-discontinuities (i.e. 30, 60 and 90 μs in Figure 17a) are clearly visible, while for PAPR = 2.0 (red line), the peaks disappear (see also Figure 17b at 30, 60 and 90 μs).

Figures 18a and 18b show the estimated bandwidth reducing the SNR at 10 and 5 dB, with natural PAPR, respectively. In the latter case, not all time-discontinuities are clearly detectable.

For a noise waveform generated by COSPAR, with the same parameters, that is, $B = 50$ MHz, Blackman–Nuttall spectral window, SNR = 40 dB, $T_i = 30$ μs, $p = 4$, natural PAPR and PAPR = 2.0, Figures 19a and 19b show the PSWVD in similar way as in Figures 17a and 17b. In this case, natural PAPR and PAPR = 2.0 are very similar and no time-discontinuity is visible. This is confirmed in Figure 19c, where the estimated bandwidth shows the same oscillating values without peaks in correspondence of the sub-pulses. This effect is due to the constant power spectrum of the COSPAR sub-pulses compared to the FMeth ones.

5 | SOME LIMITATIONS IN THE CLASSIFICATION OF RADAR SIGNALS BY TFD—THE NOISE RADAR CASE

Artificial Intelligence (AI) and neural networks are today widely used for classification of radar signals [68]. In literature, there are dozens, if not hundreds of publications on this subject, see references of [69–71]. We underline some comments regarding the radar waveform recognition system.

(i) The TFD methods were initially developed for the analysis of non-stationary signals, whose field of application provides for a high signal-to-noise ratio, for example, for voice and image analysis, for medical applications [72] and so on, that is, in a very different context than the radar one, where the signals to be detected are normally immersed in noise.

(ii) In the frame of detection/interception/identification of LPI signals, the 2D-image of the TFD and its following processing and classifying has been applied (in the open literature) for a finite set of n (≈6–12) deterministic signals, for example, LFM signals, Costas codes, BPSK codes, Frank, P1, P2, P3 and P4 codes [33, 46–49], while the field reality shows a much richer set of radar signal types, especially in the modern context of MIMO (Multiple Input, Multiple Output) radar and of ISAC (Integrated Sensing and Communications).

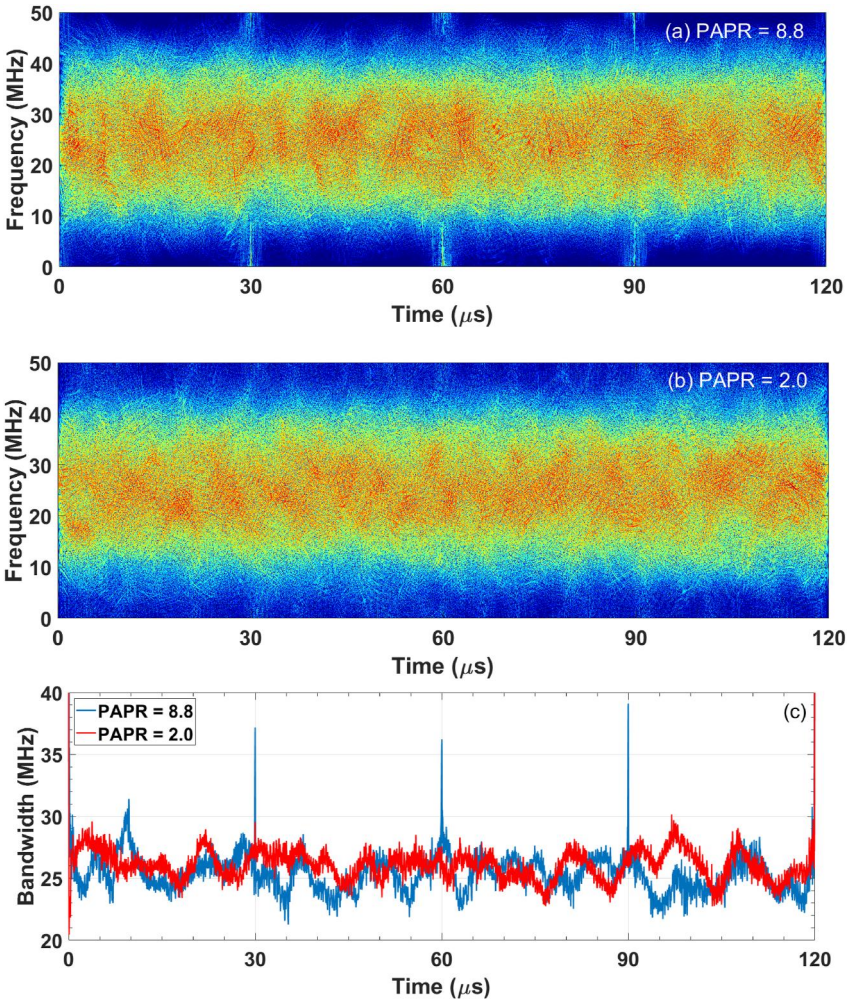

FIGURE 17 FMeth waveform, SNR = 40 dB. (a) PSWVD for natural PAPR (=8.8). (b) PSWVD for PAPR = 2.0. (c) Estimated Bandwidth by Equations (7) and (8): PAPR = 8.8 (blue), PAPR = 2.0 (red).

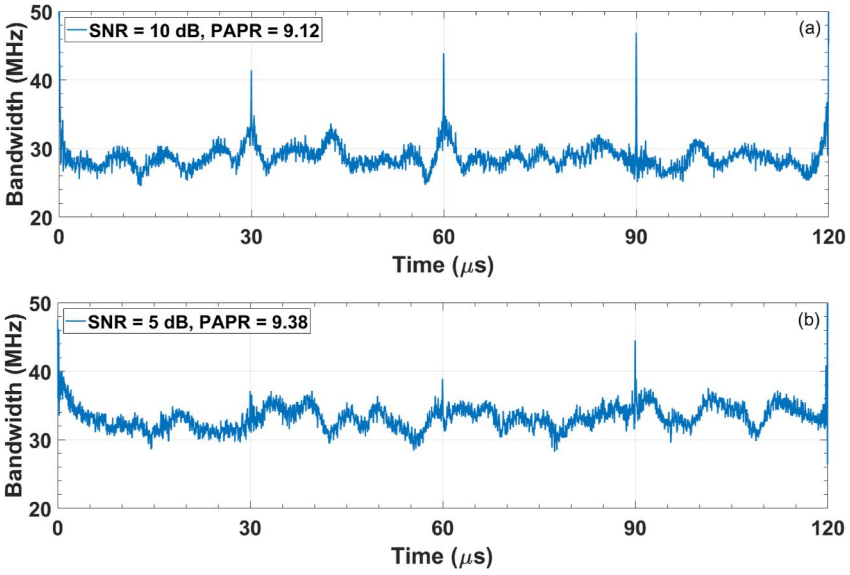

FIGURE 18 FMeth waveform with natural PAPR. Estimated Bandwidth. (a) SNR = 10 dB. (b) SNR = 5 dB.

(iii) Most analyses in the open literature suppose the exact knowledge of the trailing and leading edges for the intercepted radar pulse, that is, for pulse-compression radars, the rise time t_r and the fall time t_f of the modulation on pulse (MOP). In principle, this is not strictly possible unless the SNR and the bandwidth B tend to

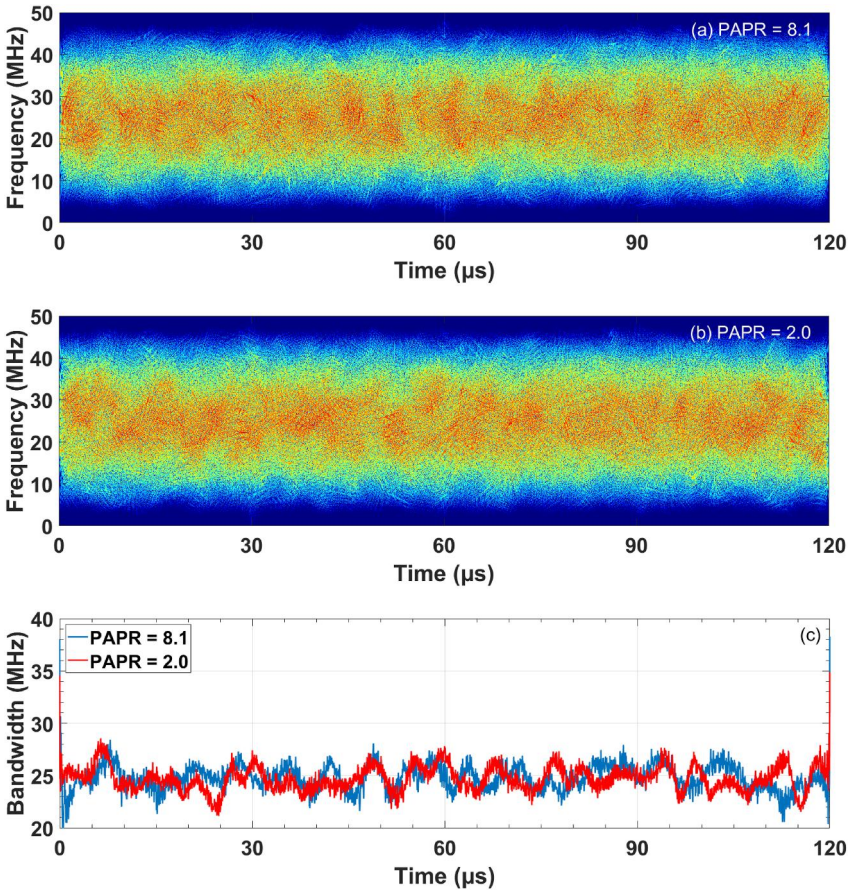

FIGURE 19 COSPAR waveform, SNR = 40 dB. (a) PSWVD for natural PAPR (=8.1). (b) PSWVD for PAPR = 2.0. (c) Estimated Bandwidth by Equations (7) and (8): PAPR = 8.1 (blue), PAPR = 2.0 (red).

infinity. In all real conditions, the pulse (uncorrupted by noise) is not rectangular but has a finite rise and fall times. The effect of the noise, added to the pulse, is to shift the time of threshold crossing of a random quantity ΔT_r, whose *rms* error is [73], chapter 6.3:

$$\delta T_r = \sqrt{\frac{T}{B \cdot SNR}} \tag{9}$$

with B the bandwidth of the IF filter, T the duration of the signal and SNR the signal to noise ratio at the output of the matched filter. The standard deviation δT_r decreases as B increases and the duration T decreases. For the simple rectangular pulse, the BT product is of the order of unity, more complex waveforms can have BT products much greater than the unit. In these cases, once T is fixed, the bands are much wider than the rectangular pulse, that is, permit a better precision. Equation (9) can be rewritten in terms of the statistical loss of samples in percentage:

$$\frac{\delta T_r}{T} = \sqrt{\frac{1}{BT \cdot SNR}} \tag{10}$$

Figure 20 shows Equation (10) for BT equal to 10^2, 10^3 and 10^4; for low SNR (−10 dB), the losses are 33%, 10% and 3%. For positive SNR (>5 dB), the loss is less than 5%. The effect

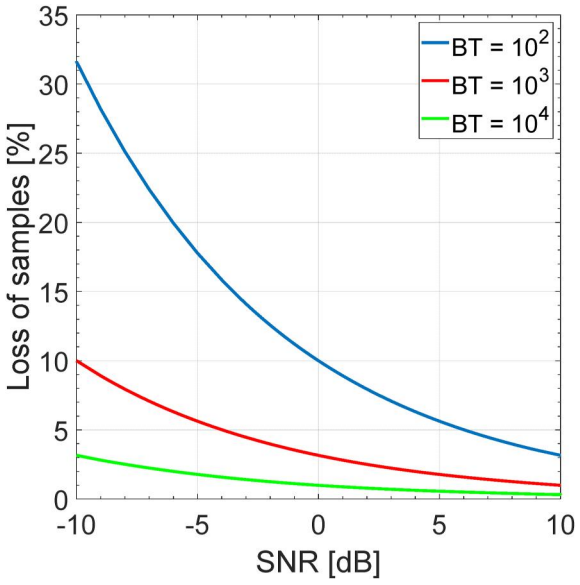

FIGURE 20 Loss of samples in percentage.

of this loss on the training of a neural network is reasonably expected to be significant.

In the Noise Radar case, it is worthy to add the following considerations.

(i) TFD seems of little (if any) use in the case of pseudo-random signals, that is, for CE Noise Radars, as the relationship between the time and instantaneous frequency is random, and the number of signal types to be classified/recognised can tend theoretically to infinity, making the *Off-line Training* of Figure 1 practically impossible.

(ii) A CE-NR waveform is characterised by the above-discussed parameters (see also section 4): central frequency f_0, B, T, *PAPR*, *PSL* and more. In defence applications, it is reasonable (and likely) to expect some degree of *agility* for f_0 (not to mention B) and *time stagger* for T, respecting the condition for the operational maximum range, that is, $\frac{cT}{2} = d \cdot R_{max}$ with an acceptable mismatching loss (e.g. equal to slightly less than 1 dB for $d = 5$). Hence, varying T by *time stagger*, for example, with *d uniform* distributed in the interval (5–6), we will prevent the correlation receiver (Figure 10) of the opponent to operate at the maximum SNR.

6 | CONCLUSIONS

From the mere anti-interception point of view, an ideal Noise Radar shall transmit a wide-bandwidth Gaussian noise with a flat power spectrum in a Continuous Emission mode to best approximate a maximal entropy (minimal interceptability and exploitability) source.

However, in the real world, practical needs and requirements limit both bandwidth B and duration T of the radar pseudorandom signal, calling for an effective exploitation of the power transmitter, that is, a PAPR as close to the unity as possible, with a signal-to-noise gain of the order of 10 dB's with respect to the Gaussian signal. Conversely, a Peak-to-Side lobe Level (PSL) better than BT is often required especially in the *close-range* interval where antenna leakage occurs. Hence, *"tailored"* pseudorandom waveforms are needed in CE Noise Radars, whose processing, necessarily applied to *"blocks"* or *"segments"* of the signal, destroys both the Gaussian statistics and the spectral flatness, thus reducing the *uncertainty* of the signal and impairing its LPI/LPE features. To evaluate these features, an *"observer"* has been defined using Time–Frequency analysis to estimate the central frequency, the bandwidth B and the duration T in different conditions that is, sidelobes reduction (spectral windows) applied or not; PAPR reduction applied or not. Note that T has been supposed constant in this work, but it is not necessarily constant in real-world applications of Noise Radar Technology, which will better resort to some *"staggering"*, similar to the PRF staggering of conventional pulse radars.

The results (see also [63]) show that

a. Detectability of Noise Radar in different receiver noise levels (different SNR's) does not depend on the particular *"tailoring"* of the pseudorandom signal that is, it is practically the same with the PAPR reduction applied or not and the PSL controlled or not.

b. The bandwidth estimation may be used to evaluate T when the side lobe suppression (SLS) function is applied, that is, for FMeth generator. However, the estimation of T is feasible with a large enough (at least 5 dB or 10 dB) SNR.

c. The COSPAR generator, for the more regularity of the sub-pulses (i.e. absence of the SLS algorithm), appears more robust to the estimation of T; however, its intrinsic weakness is that all noise waveforms have the same spectrum.

In spite of the powerful time–frequency analysis (section 5 and Appendix A) and the more and more widespread use of Artificial Intelligence (AI), the well-known techniques of frequency agility and time staggering would make the estimate of B and T much more difficult and significantly improve the LPD/LPI/LPE features of CE Noise Radars: This point is worth of future research.

AUTHOR CONTRIBUTIONS

Gaspare Galati: Conceptualisation; formal analysis; methodology; supervision. **Gabriele Pavan**: Data curation; formal analysis; software; writing – original draft.

CONFLICT OF INTEREST STATEMENT

The authors have not conflict of interest.

DATA AVAILABILITY STATEMENT

Data available on request from the authors.

ORCID

Gaspare Galati https://orcid.org/0000-0003-1805-4640
Gabriele Pavan https://orcid.org/0000-0002-5318-7265

REFERENCES

1. Adamy, D.: EW104–EW against New Generation of Threats. Artech House, Inc., Norwood (2015)
2. De Martino, A.: Introduction to Modern EW Systems, 2nd ed. Artech House, Inc., Norwood (2018)
3. Robertson, S.: Practical ESM Analysis. Artech House, Norwood (2019)
4. O'Donoghue, N.A.: Emitter Detection and Geolocation for Electronic Warfare. Artech House, Norwood (2020). ISBN 978-1-63081-564-6
5. Pace, P.E.: Detecting and Classifying LPI Radar, 2nd ed. Artech House, Norwood (2009)
6. Long, X., et al.: Ambiguity function analysis of random frequency and PRI agile signals. IEEE Trans. Aero. Electron. Syst. 57(1), 382–396 (2021). https://doi.org/10.1109/taes.2020.3016851
7. Kulpa, K.: Noise Radar. Artech House, Nowood MA (2013). ISBN 978-1-60807-661-1
8. De Palo, F., et al.: Introduction to noise radar and its waveforms. MDPI Sensors 20(18), 5187 (2020). https://doi.org/10.3390/s20185187
9. Galati, G., Pavan, G., Wasserzier, C.: Signal design and processing for noise radar. Eurasip JASP 2022(1), 52 (2022). Published on: 21 June 2022. https://doi.org/10.1186/s13634-022-00884-1
10. Galati, G., et al.: Counter-interception and counter-exploitation features of noise radar Technology. MDPI Remote Sens. 13(22), 4509 (2021). https://doi.org/10.3390/rs13224509
11. Cover, T.M., Thomas, J.A.: Elements of Information Theory, 2nd ed. John Wiley & Sons, Inc., Hoboken, NJ, USA (2006)
12. Dubnov, S.: Generalization of spectral flatness measure for non-Gaussian linear processes. IEEE Signal Process. Lett. 11(8), 698–701 (2004). https://doi.org/10.1109/lsp.2004.831663

13. NIST Glossary (Online) https://csrc.nist.gov/glossary/term/prng
14. Matsumoto, M., Nishimura, T.: Mersenne Twister: a 623-dimensionally equidistributed uniform pseudo-random number generator. ACM Trans. Model Comput. Simulat 8(1), 3–30 (1998). https://doi.org/10.1145/272991.272995
15. Smith, G.E., Reininger, T.J.: Reinforcement learning for waveform design. In: IEEE Radar Conference (RadarConf21). Atlanta (2021). https://doi.org/10.1109/RadarConf2147009.2021.9455187
16. Baietto, A., et al.: Lean neural networks for autonomous radar waveform design. Sensors 22(4), 1317 (2022). https://doi.org/10.3390/s22041317
17. Coutino, M., Uysal, F.: Reinforcement learning for radar waveform optimization. In: IEEE Radar Conference (RadarConf23). San Antonio (2023). https://doi.org/10.1109/RadarConf2351548.2023.10149794
18. Thayaparan, T., Daković, M., Stanković, L.: Mutual interference and low probability of interception capabilities of noise radar. IET Radar. Sonar Navig. 2(4), 294–305 (2008). https://doi.org/10.1049/iet-rsn:20070146
19. Shastry, M., Narayanan, R., Rangaswamy, M.: Sparsity-based signal processing for noise radar imaging. IEEE Trans. Aero. Electron. Syst. 51(1), 314–325 (2015). https://doi.org/10.1109/TAES.2014.130733
20. Cohen, L.: Time-Frequency Analysis: Theory and Applications. Pearson College Div (1995). ISBN: 9780135945322
21. Boashash, B.: Time-Frequency Signal Analysis and Processing, 2nd ed. Academic Press (2015). ISBN: 9780123984999
22. Wigner, E.P.: On the quantum correction for thermodynamic equilibrium. Phys. Rev. 40(5), 749–759 (1932). https://doi.org/10.1103/physrev.40.749
23. Gabor, D.: Theory of communication. Part 1: the analysis of information. J. Inst. Eng. Electron. 93(26), 429–441 (1946). https://doi.org/10.1049/ji-3-2.1946.0074
24. Ville, J.: Theorie et applications de la notion de signal analytique. Cables Transm. 2A, 61–74 (1948)
25. Cohen, L.: Time-frequency distributions-A review. Proc. IEEE 77(N. 7), 941–981 (1989). https://doi.org/10.1109/5.30749
26. Choi, H., Williams, W.J.: Improved time-frequency representation of multicomponent signals using exponential kernels. IEEE Trans. Acoust. Speech Signal Process. 37(6), 862–871 (1989). https://doi.org/10.1109/assp.1989.28057
27. O' Toole, J.M., Boashash, B.: Fast and memory-efficient algorithms for computing quadratic time-frequency distributions. Appl. Comput. Harmon. Anal. 35(2), 350–358 (2013). https://doi.org/10.1016/j.acha.2013.01.003
28. Zhang, M., Liu, L., Diao, M.: LPI radar waveform recognition based on time-frequency distribution. MDPI Sensors 16(10), 1682 (2016). https://doi.org/10.3390/s16101682
29. Nixon, M., Aguado, A.: Feature Extraction and Image Processing for Computer Vision, 4th ed. Academic Press (2019). ISBN: 9780128149768
30. Boashash, B.: Estimating and interpreting the instantaneous frequency of a signal. I Fundamentals. Proc. IEEE 80(4), 520–538 (1992). https://doi.org/10.1109/5.135376
31. Boashash, B.: Estimating and interpreting the instantaneous frequency of a signal II. Algorithms and Applications. Proc. IEEE 80(4), 540–568 (1992). https://doi.org/10.1109/5.135378
32. Matuszewski, J., Pietrow, D.: Specific radar recognition based on characteristics of emitted radio waveforms using convolutional neural networks. MDPI Sensors 21(24), 8237 (2021). https://doi.org/10.3390/s21248237
33. Wang, C., Wang, J., Zhang, X.: Automatic radar waveform recognition based on time-frequency analysis and convolutional neural network. In: 2017 IEEE International Conference on Acoustics, Speech and Signal Processing (ICASSP), pp. 2437–2441. New Orleans (2017)
34. Wang, Q., et al.: Transferred deep learning based waveform recognition for cognitive passive radar. Signal Process. 155(2019), 259–267 (2019). https://doi.org/10.1016/j.sigpro.2018.09.038
35. Jordanov, I., Petrov, N., Petrozziello, A.: Supervised radar signal classification. In: International Joint Conference on Neural Networks, pp. 24–29. Vancouver (2016). https://doi.org/10.1109/IJCNN.2016.7727371
36. Pan, Z., et al.: Automatic waveform recognition of overlapping LPI Radar Signals based on Multi-Instance multi-label learning. IEEE Signal Process. Lett. 27, 1275–1279 (2020). https://doi.org/10.1109/lsp.2020.3009195
37. Wang, G., et al.: Radar emitter sorting and recognition based on time-frequency image union feature. In: IEEE 4th International Conference on Signal and Image Processing (ICSIP). Wuxi, China (2019). https://doi.org/10.1109/SIPROCESS.2019.8868524
38. Zhou, X.W., Tian, Y., Wang, R.: A novel radar signal recognition method based on a deep restricted Boltzmann machine. Eng. Rev. 37(2), 165–171 (2017)
39. Geng, Z., et al.: Deep-learning for radar: a survey. IEEE Access 9, 141800–141818 (2021). https://doi.org/10.1109/ACCESS.2021.3119561
40. Si, W., Luo, J., Deng, Z.: Multi-label hybrid radar signal recognition based on a feature pyramid network and pyramid network and class activation mapping. IET Radar, Sonar Navig. 16(5), 786–798 (2022). https://doi.org/10.1049/rsn2.12220
41. Zhang, X., et al.: Radar signal intrapulse modulation recognition based on a denoising-guided disentangled network. MDPI Remote Sens. 14(5), 1252 (2022). https://doi.org/10.3390/rs14051252
42. Ghayour Bhatti, S., Iqbal Bhatti, A.: Radar signals intrapulse modulation recognition using phase-based STFT and BiLSTM. IEEE Access 10, 80184–80194 (2022). https://doi.org/10.1109/ACCESS.2022.3195273
43. Wan, T., et al.: Deep learning-based LPI radar signals analysis and identification using a Nyquist Folding Receiver architecture. Defence Technol. 19, 196–209 (2023). https://doi.org/10.1016/j.dt.2021.09.019
44. Chilukuri, R.K., Kakarla, H.K., Subba Rao, K.: Radar signal recognition based on multilayer perceptron neural network. Int. J. Electr. Comput. Eng. Syst. 14(1), 29–36 (2023). https://doi.org/10.32985/ijeces.14.1.4
45. Bobin, J., et al.: Morphological component analysis: an adaptive thresholding strategy. IEEE Trans. Image Process. 16(Issue 11), 2675–2681 (2007). https://doi.org/10.1109/TIP.2007.907073
46. Gulum, T.O., et al.: A parameter extraction technique for FMCW radar signals using Wigner-Hough-Radon transform. In: IEEE Radar Conference. Atlanta (2012). https://doi.org/10.1109/RADAR.2012.6212255
47. Erdogan, A.Y., et al.: FMCW signal detection and parameter extraction by cross Wigner-Hough transform. IEEE Trans. Aero. Electron. Syst. 53(N), 334–344 (2017). https://doi.org/10.1109/taes.2017.2650518
48. Willetts, B., Ritchie, M., Griffiths, H.: Optimal time-frequency distribution selection for LPI radar pulse classification. In: IEEE International Radar Conference, pp. 28–30. Washington (2020). https://doi.org/10.1109/RADAR42522.2020.9114598
49. Guner, K.K., Gulum, T.O., Erkmen, B.: FPGA-based Wigner-Hough transform system for detection and parameter extraction of LPI radar LFMCW signals. IEEE Trans. Instrum. Meas. 70, 1–15 (2021). https://doi.org/10.1109/tim.2021.3060584
50. Galati, G., Pavan, G.: Optimal chirp waveforms for long/medium range surveillance radar. In: Proceedings of the16th International Radar Symposium, pp. 23–26. Dresden, Germany (2015). https://doi.org/10.1109/IRS.2015.7226308
51. Govoni, M.A., Li, H., Kosinski, J.A.: Low probability of interception of an advanced noise radar waveform with linear-FM. IEEE Trans. Aero. Electron. Syst. 49(N), 1351–1356 (2013). https://doi.org/10.1109/taes.2013.6494419
52. Pralon, L., Pompeo, B., Fortes, J.M.: Stochastic analysis of random frequency modulated waveforms for noise radar systems. IEEE Trans. Aero. Electron. Syst. 51(Issue 2), 1447–1461 (2015). https://doi.org/10.1109/TAES.2014.140072
53. Kulpa, J.S.: Mismatched filter for range sidelobes suppression of pseudo-noise signals. In: Proceedings of the Signal Processing Symposium (SPSympo) 2015. Debe, Poland (2015)
54. Savci, K., Galati, G., Pavan, G.: Low-PAPR waveforms with shaped spectrum for enhanced low probability of intercept noise radars special Issue - advances of noise radar for remote sensing (ANR-RS). MDPI Remote Sens. 13(12), 2372 (2021). https://doi.org/10.3390/rs13122372

55. Jakabosky, J., Blunt, S.D.: Waveform design and receive processing for nonrecurrent nonlinear FMCW radar. In: Proceedings of IEEE Radar Conference (RadarCon). Arlington (2015). https://doi.org/10.1109/RADAR.2015.7131210
56. Ravenscroft, B., et al.: Analysis of spectral notching in FM noise radar using measured interference. In: International Conference on Radar Systems (Radar 2017), pp. 23–26. Belfast (2017). https://doi.org/10.1049/cp.2017.0388
57. Blunt, S.D.: Time-frequency analysis of spectrally-notched random FM waveforms. In: 2020 IEEE International Radar Conference (RADAR), pp. 28–30. Washington (2020). https://doi.org/10.1109/RADAR42522.2020.9114585
58. Houghton, A.W., Reeve, C.D.: Detection of spread-spectrum signals using the time-domain filtered cross spectral density. IEE Proc. Radar, Sonar Navig. 142(6), 286–292 (1995). https://doi.org/10.1049/ip-rsn:19952150
59. Houghton, A.W., Reeve, C.D.: Direction finding on spread-spectrum signals using the time-domain filtered cross spectral density. IEE Proc. Radar, Sonar Navig. 144(6), 315–320 (1997). https://doi.org/10.1049/ip-rsn:19971397
60. Ardoino, R., Megna, A.: LPI Radar detection: SNR performances for a dual channel Cross-Correlation based ESM Receiver. In: Proceedings of the European Radar Conference (EuRAD 2009), pp. 113–116. Rome (2009)
61. Galati, G., Pavan, G.: Measuring the Anti-Intercept features of Noise Radar waveforms: the way ahead. In: IEEE 9th International Workshop on Metrology for AeroSpace, pp. 27–29. Pisa, Italy (2022). https://doi.org/10.1109/MetroAeroSpace54187.2022.9856112
62. Galati, G., Pavan, G., Wasserzier, C.: Interception of continuous-emission noise radars transmitting different waveform configurations. In: 23rd International Radar Symposium, pp. 12–14. Gdansk (2022). https://doi.org/10.23919/IRS54158.2022.9904981
63. Galati, G., Pavan, G.: Continuous-emission noise radars: interception and extraction of waveform parameters. In: IEEE Conference SPSympo 2023, pp. 26–28. Karpacz, Poland (2023). accepted to the
64. Heino, M., et al.: Theoretical and experimental analysis of the supposed stealthiness of noise radar. In: Proceedings of IEEE Radar Conference (RadarConf23). San Antonio (2023). https://doi.org/10.1109/RadarConf2351548.2023.10149654
65. Wasserzier, C., Galati, G.: On the efficient computation of range and Doppler data in noise radar. Int. J. Microw. Wirel. Technol. 11(7), 584–592 (2019). https://doi.org/10.1017/S175907871800171X
66. Muehe, C.E.: The moving target detector. IEEE Trans. Aero. Electron. Syst. 42(3), 1177–1181 (2006). https://doi.org/10.1109/TAES.2006.248219
67. Galati, G., Pavan, G., Wasserzier, C.: Signal Processing Symposium (SPSympo) 2019. Krakow (2019). https://doi.org/10.1109/SPS.2019.8882098
68. Haigh, K., Andrusenko, J.: Cognitive Electronic Warfare: An Artificial Intelligence Approach. Artech House (2021)
69. Xiao, Z., Yan, Z.: Radar emitter identification based on novel time-frequency spectrum and convolutional neural network. IEEE Commun. Lett. 25(8), 2634–2638 (2021). https://doi.org/10.1109/LCOMM.2021.3084043
70. Wang, X., et al.: Convolutional neural network applied to specific emitter identification based on pulse waveform images. IET Radar Sonar Navig. 14(5), 728–735 (2020). https://doi.org/10.1049/iet-rsn.2019.0456
71. Qu, Z., et al.: Radar signal intra-pulse modulation recognition based on convolutional neural network and deep Q-learning network. IEEE Access 8, 49125–49136 (2020). https://doi.org/10.1109/ACCESS.2020.2980363
72. Ricamato, A.L., et al.: A time-frequency approach to evaluate electromyographic recordings. In: Proceedings Fifth Annual IEEE Symposium on Computer-Based Medical Systems, pp. 14–17. Durham (1992). https://doi.org/10.1109/CBMS.1992.245010
73. Skolnik, M.I.: Introduction to Radar Systems, 3rd ed. McGraw-Hill (2001). Chapter 6.3

How to cite this article: Galati, G., Pavan, G.: On the anti-intercept features of noise radars. IET Radar Sonar Navig. 1–22 (2023). https://doi.org/10.1049/rsn2.12504

APPENDIX A

Time/frequency representation of a signal

A.1 Time/frequency correlation function, complex ambiguity function and wigner distribution

Defining the instantaneous *time correlation* as follows:

$$R(t,\tau) = s\left(t+\frac{\tau}{2}\right)s^*\left(t-\frac{\tau}{2}\right) \ \forall \ t,\tau \tag{A.1}$$

where the variable t is the *absolute time*, while τ is the *relative time* or *"the time lag"*, the Fourier transform on t of $R(t,\tau)$ defines the *complex ambiguity function*:

$$\chi(\tau,\nu) = \mathscr{F}_t\{R(t,\tau)\} = \int s\left(t+\frac{\tau}{2}\right)s^*\left(t-\frac{\tau}{2}\right)e^{-j2\pi\nu t}dt \ \forall \ \tau,\nu \tag{A.2}$$

whose amplitude is the Woodward's ambiguity function for the radar waveform having complex envelope $s(t)$:

$$\begin{aligned}|\chi(\tau,\nu)| &= \left|\int_{-\infty}^{+\infty} s\left(t+\frac{\tau}{2}\right)s^*\left(t-\frac{\tau}{2}\right)e^{-j2\pi\nu t}\,dt\right| \\ &= \left|\int_{-\infty}^{+\infty} s(t)s^*(t+\tau)e^{j2\pi\nu t}dt\right|\end{aligned} \tag{A.3}$$

When the Fourier transform is evaluated on τ, it is defined as the Wigner distribution function:

$$W_s(t,f) = \mathscr{F}_\tau\{R(t,\tau)\} = \int s\left(t+\frac{\tau}{2}\right)s^*\left(t-\frac{\tau}{2}\right)e^{-j2\pi f\tau}d\tau \ \forall \ t,f \tag{A.4}$$

The main properties of the Wigner distribution are

(i) $W_s(t,f)$ is a real function, that is, $W_s^*(t,f) = W_s(t,f)$, even if $s(t)$ is a complex signal.
(ii) For real signals, it is symmetrical in the frequency domain, that is, $W_s(t,-f) = W_s(t,f)$.
(iii) It is time-shift and frequency-shift invariant, that is,
if $g(t) = s(t-t_0)$ then $W_g(t,f) = W_s(t-t_0,f)$
if $g(t) = s(t)e^{j2\pi f_0 t}$ then $W_g(t,f) = W_s(t,f-f_0)$.
(iv) Time and frequency marginal property states that

$$\int W_s(t,f)df = |s(t)|^2; \int W_s(t,f)dt = |S(f)|^2$$

Hence, the energy of the signal is

$$E = \int\int W_s(t,f)dtdf = \int |s(t)|^2 dt = \int |S(f)|^2 df$$

Introducing the instantaneous frequency correlation of $s(t)$

$$A(f,\nu) = S\left(f+\frac{\nu}{2}\right)S^*\left(f-\frac{\nu}{2}\right) \;\forall\; \nu,f \qquad (A.5)$$

with $S(f)$ the Fourier transform of $s(t)$, Equation (A.5) enables the interpretation of f as the *absolute frequency*, while ν is the *relative frequency* or frequency shift. $A(f,\nu)$ can be obtained by the 2D-Fourier transform on t and τ of $R(t,\tau)$:

$$A(f,\nu) = \mathcal{F}_{t,\tau}\{R(t,\tau)\} = \iint R(t,\tau)e^{-j2\pi(\nu t+f\tau)}dtd\tau \;\forall\; \nu,f \qquad (A.6)$$

Introducing Equation (A.1) in Equation (A.6), by Equation (A.2) and Equation (A.4), the instantaneous frequency correlation function $A(f,\nu)$ can be written in terms both of the Wigner distribution or the complex ambiguity function:

$$A(f,\nu) = \mathcal{F}_t\{W(t,f)\} = \int W(t,f)e^{-j2\pi\nu t}dt \qquad (A.7a)$$

$$A(f,\nu) = \mathcal{F}_\tau\{\chi(\tau,\nu)\} = \int \chi(\tau,\nu)e^{-j2\pi f\tau}dt \qquad (A.7b)$$

From Equation (A.7), the Wigner distribution and the complex ambiguity function are related to each other as follows:

$$W(t,f) = \iint \chi(\tau,\nu)e^{-j2\pi(f\tau-\nu t)}d\tau d\nu \qquad (A.8a)$$

$$\chi(\tau,\nu) = \iint W(t,f)e^{-j2\pi(\nu t-f\tau)}dtdf \qquad (A.8b)$$

Figure A1 shows the relationships among the four bi-dimensional functions $R(t,\tau)$, $A(f,\nu)$, $\chi(\tau,\nu)$ and $W(t,f)$.

A.2 Wigner–Ville Distribution (WVD) function

In 1948 J. A. Ville introduced a complex signal, said *analytic* signal $z(t)$, to represent a real (physical) signal $s_R(t)$. If $s_R(t)$ is a base-band signal with spectrum $S(f)$, the related analytic signal is

$$z(t) = s_R(t) + j\mathcal{H}\{s_R(t)\} \qquad (A.9)$$

where the real part of $z(t)$ is $s_R(t)$, while the imaginary part is the Hilbert transform of $s_R(t)$, that is, the output of a filter with impulse response $h_H(t) = \frac{1}{\pi t}$. The spectrum of $z(t)$, that is, $Z(f)$, is *zero* for negative frequencies and equal to $S(f)$ for positive frequencies. The Wigner distribution, evaluated using the analytic signal $z(t)$ of Equation (A.9) instead of $s(t)$ in Equation (A.4), is usually applied in practice today and is called the *Wigner–Ville Distribution* (WVD). There are several advantages using the analytic signal in the Wigner distribution.

(i) From Equation (A.4), the Wigner distribution is a quadratic functional of $s(t)$, hence, it produces interferences between the negative and positive frequency components of the signal, which are absent if $z(t)$ is used.
(ii) The analytic signal guarantees that the first moment of the Wigner–Ville distribution is the instantaneous frequency, that is, the time derivative of the phase.
(iii) Numerical algorithms for the computation of the Wigner distribution will have to rely on oversampling the original waveform to avoid serious aliasing in the frequency domain; using the analytic signal, and no oversampling is required.

The WVD has the best possible concentration, but the presence of the *cross terms*, that is, of large oscillating terms located in the middle between the actual signal components, affects its results. Because the WVD is a quadratic functional of the signal $s(t)$, when $s(t)$ is a multicomponent signal, for example, $s(t) = s_1(t) + s_2(t)$, the Wigner distribution results in the sum of four terms:

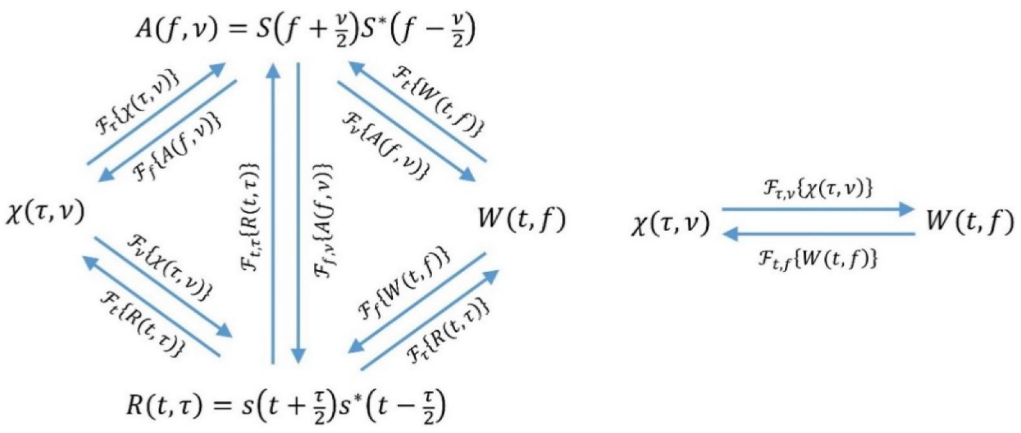

FIGURE A1 Relationship among the four bi-dimensional functions $R(t,\tau)$, $A(f,\nu)$, $\chi(\tau,\nu)$ and $W(t,f)$.

$$W(t,f) = W_{s1}(t,f) + W_{s2}(t,f) + W_{s1s2}(t,f) + W_{s2s1}(t,f)$$

The presence of the two cross terms $W_{s1s2}(t,f)$ and $+W_{s2s1}(t,f)$ poses a serious problem on the use of the Wigner distribution, and the methods to minimise the contribution of these terms must be employed.

The Cohen's class representation [25] allows us to reduce the cross terms with limited effects on the useful properties of the WVD. The Cohen's class can be thought as a 2D linear filtering in time/frequency by the functions $g_1(t)$ and $G_2(f)$ respectively, leading to the Pseudo-Smoothed Wigner–Ville distribution (i.e. with smoothing both in time and in frequency):

$$W^{PS}(t,f) = g_1(t) * W(t,f) * G_2(f) \tag{A.10}$$

where $W(t,f)$ is the Wigner–Ville distribution and the '*' denotes the convolution operator. If $G_1(\nu) = 1$, that corresponds at $g_1(t) = \delta(t)$, Equation (A.10) becomes the Pseudo Wigner–Ville distribution smoothed only in the frequency domain, on the other hand, when $g_2(\tau) = 1$, that corresponds at $G_2(f) = \delta(f)$, the Equation (A.10) becomes the Wigner–Ville distribution only smoothed in time.

APPENDIX B

Detection test for a pseudorandom signal of interest

Denoting with $\boldsymbol{s}$ the signal of interest (SOI) and with $\boldsymbol{n}_1$, $\boldsymbol{n}_2$ the noise of the two receivers (see Figure 10 in section 3), the detection procedure of the 2A&C receiver is defined by the following binary hypothesis test:

$$H_0 : \begin{cases} \boldsymbol{y_1} = \boldsymbol{n_1} \\ \boldsymbol{y_2} = \boldsymbol{n_2} \end{cases} H_1 : \begin{cases} \boldsymbol{y_1} = \boldsymbol{s} + \boldsymbol{n_1} \\ \boldsymbol{y_2} = a \cdot \boldsymbol{s} + \boldsymbol{n_2} \end{cases} \tag{B.1}$$

with a a complex constant describing the differential attenuation and the phase shift of the receiving paths, including the delay between the antennas (which, however, are very close, of the order of less than 1 m in practical applications). Hence, here, we set $a = 1$. Under this assumption, the output from the cross-correlator to test is only the zero-lag term R of the cross-correlation between $\boldsymbol{y}_1$ and $\boldsymbol{y}_2$:

$$R = \boldsymbol{y_1}^H \cdot \boldsymbol{y_2} \tag{B.2}$$

where H denotes the Hermitian-transpose operator.

Under the *null hypothesis* H_0, $\boldsymbol{y}_1 = \boldsymbol{n}_1$ and $\boldsymbol{y}_2 = \boldsymbol{n}_2$ are independent and Gaussian distributed complex vectors with *zero mean* and equal covariance matrix (diagonal with elements σ_n^2). The closed form of the distribution of $R = \boldsymbol{n_1}^H \boldsymbol{n_2}$ is not available, making it difficult to set the decision threshold η versus the probability of false alarm (P_{FA}). However, the distribution of $\boldsymbol{n_1}^H \boldsymbol{n_2}$ for a sufficient length of the vectors, thanks to the *Central Limit theorem*, is (with a good approximation) Gaussian with *zero mean* and variance $\sigma_0^2 = \frac{N^2 T_{corr}}{B_n}$, where N is the noise power in the bandwidth band B_n of the receivers and T_{corr} is the time of correlation that we suppose is equal to the duration T of the signal of interest $\boldsymbol{s}$.

Under the *alternative hypothesis* H_1, expanding Equation (B.2), R is the sum of four terms:

$$R = \boldsymbol{s}^H \boldsymbol{s} + \boldsymbol{s}^H \boldsymbol{n_2} + \boldsymbol{n_1}^H \boldsymbol{s} + \boldsymbol{n_1}^H \boldsymbol{n_2} \tag{B.3}$$

Deterministic case. If the signal of interest $\boldsymbol{s}$ is deterministic, the term $\boldsymbol{s}^H \boldsymbol{s}$ is equal to the energy $S \cdot T$, where S is the signal power entering the filter and T the duration of $\boldsymbol{s}$. The two cross terms $\boldsymbol{s}^H \boldsymbol{n}_2$ and $\boldsymbol{n}_1^H \boldsymbol{s}$ are Gaussian-distributed complex random variables with *zero mean* and variance equal to $\frac{NST}{B_n}$, while the distribution of $\boldsymbol{n}_1^H \boldsymbol{n_2}$ is Gaussian-distributed with *zero mean* and variance $\frac{N^2 T}{B_n}$. Summing up in the presence of a deterministic signal $\boldsymbol{s}$, the test statistics R, Equation (B.3), is a complex Gaussian random variable with mean ST and variance: $\sigma_R^2 = \frac{N^2 T}{B_n} + \frac{2NST}{B_n} = \frac{NT}{B_n}(N+2S)$. Hence, the signal-to-noise ratio at the output is

$$SNR_0 = \frac{S^2 T^2}{\frac{NT}{B_n}(N+2S)} = \frac{B_n T S^2}{N^2 + 2NS} = B_n T \frac{SNR_i^2}{1 + 2 \cdot SNR_i} \tag{B.4}$$

being $SNR_i = \frac{S}{N}$ the signal-to-noise ratio at the input of the receiver.

Pseudorandom case. For a pseudorandom signal $\boldsymbol{s}$, the cross-correlation R, applying the *Central Limit theorem*, is distributed as a complex Gaussian random variable with mean ST and variance $\sigma_R^2 = \frac{N^2 T}{B_n} + \frac{2NST}{B_n} + \frac{2S^2 T}{B_n}$. The added term $\frac{2S^2 T}{B_n}$ takes into account the randomicity of $\boldsymbol{s}$. Hence, the corresponding SNR_0 becomes

$$SNR_0 = \frac{S^2 T^2}{\frac{T}{B_n}(N^2 + 2NS + 2S^2)} = B_n T \frac{S^2}{(N^2 + 2NS + 2S^2)} = B_n T \frac{SNR_i^2}{1 + 2 \cdot SNR_i + 2 \cdot SNR_i^2} \tag{B.5}$$

If we assume in Equation (B.4) and Equation (B.5) B_n equal to the signal bandwidth B, the product $B_n T = BT$ is the gain (or pulse compression gain) of the coherent processing, that is, the matched filtering.

In the presence of SOI, both the mean and the variance of R depend on the strength of the signal, that is, they will change under the null (H_0) and the alternative (H_1) hypothesis, and the optimal detector is *quadratic*.

In general, for spread spectrum and/or NRT signals, the strength of the signal (S) is often much weaker than the noise one (N). Thus, the variance of R is approximately constant $\left(\sigma_R^2 \cong \sigma_0^2 = \frac{N^2 T}{B_n}\right)$, and the use of a simple threshold test is convenient in comparison with the truly optimal detector that would utilise the likelihood ratio $L(\boldsymbol{y}_1, \boldsymbol{y}_2) = f(\boldsymbol{y}_1, \boldsymbol{y}_2 | H_1) / f(\boldsymbol{y}_1, \boldsymbol{y}_2 | H_0)$.

In addition, to avoid that the mean of R depends on the unknown phase shift between the two received signal, the statistical test used for the detection is the magnitude squared of R normalised by the noise σ_0^2.

$$z(\boldsymbol{y_1}, \boldsymbol{y_2}) = \frac{2}{\sigma_0^2}\left|\boldsymbol{y_1}^H \cdot \boldsymbol{y_2}\right|^2 = \frac{2}{\sigma_0^2}|R|^2 \tag{B.6}$$

Under H_0, the statistic is

$$z_{H_0}(\boldsymbol{y_1}, \boldsymbol{y_2}) = z(\boldsymbol{y_1}, \boldsymbol{y_2}) = \frac{2}{\sigma_0^2}|R|^2 \tag{B.7}$$

The statistic z_{H_0}, being the square of a zero-mean complex Normal random variable with *unit* variance (due to the normalisation factor $2/\sigma_0^2$), is distributed as a *chi square* variable with 2 degrees of freedom (the signal $\boldsymbol{y}_1$,$\boldsymbol{y}_2$ are complex), that is, an Exponential law of parameter 0.5 with distribution $F(z|H_0) = 1 - e^{-\frac{z}{2}}$ for $z > 0$. The probability of a false alarm is easily computed as $P_{FA} = e^{-\frac{1}{2}\eta}$ and the decision threshold is

$$\eta = -2 \cdot ln(P_{FA}) \tag{B.8}$$

Under H_1, the statistics is

$$z_{H_1}(\boldsymbol{y_1}, \boldsymbol{y_2}) = \frac{2}{\sigma_1^2}|R|^2 \tag{B.9}$$

being $\sigma_1^2 = \beta \cdot \sigma_0^2$, with $\beta = 1 + 2 \cdot SNR_i$ for a deterministic signal and $\beta = 1 + 2 \cdot SNR_i + 2 \cdot SNR_i^2$ for a pseudorandom signal, Equation (B.9) becomes

$$z_{H_1}(\boldsymbol{y_1}, \boldsymbol{y_2}) = \frac{2}{\sigma_1^2}|R|^2 = \frac{1}{\beta} \cdot \frac{2}{\sigma_0^2}|R|^2 = \frac{1}{\beta} \cdot z(\boldsymbol{y_1}, \boldsymbol{y_2}) \tag{B.10}$$

The statistic z_{H_1}, being the square of a complex Normal variable R with mean $E[R] \neq 0$ and *unit* variance (due to the normalisation factor $2/\sigma_1^2$), results are distributed as a *non-central chi square* random variable with 2 degrees of freedom, where the *non-centrality parameter* (λ) can be evaluated from the mean of $|R|^2$. In fact, starting from $R = \boldsymbol{s}^H\boldsymbol{s} + \boldsymbol{s}^H\boldsymbol{n_2} + \boldsymbol{n_1}^H\boldsymbol{s} + \boldsymbol{n_1}^H\boldsymbol{n_2}$:

$$\begin{aligned} E\left[|R|^2\right] &= Var[R] + E[R]^2 = \sigma_1^2 + S^2T^2 \\ &= \sigma_0^2 \cdot \beta + \frac{S^2}{N^2}\frac{N^2T}{B_n}B_nT = \sigma_0^2 \cdot \beta + SNR_i^2 \cdot \sigma_0^2 \cdot B_nT \end{aligned}$$

with $\sigma_0^2 = \frac{N^2T}{B_n}$. With $B_nT \cdot SNR_i^2 = \beta \cdot SNR_0$, we have

$$E\left[|R|^2\right] = \sigma_0^2 \cdot \beta(1 + SNR_0) = \sigma_1^2(1 + SNR_0)$$

The mean of z_{H_1} becomes

$$E[z_{H_1}] = \frac{2}{\sigma_1^2}E\left[|R|^2\right] = 2 + 2 \cdot SNR_0 \tag{B.11}$$

For a *non-central chi square* random variable with 2 degrees of freedom, the mean and the *non-centrality parameter* λ are related as $E[z_{H_1}] = 2 + \lambda$; hence, $\lambda = 2 \cdot SNR_0$. Then, the probability of detection results are as follows:

$$\begin{aligned} P_D &= P\{z(\boldsymbol{y_1}, \boldsymbol{y_2}) > \eta\} = P\left\{z_{H_1}(\boldsymbol{y_1}, \boldsymbol{y_2}) > \frac{\eta}{\beta}\right\} \\ &= 1 - F_{\chi_2^2}\left\{x = \frac{\eta}{\beta}; \lambda = 2 \cdot SNR_0\right\} \end{aligned} \tag{B.12}$$

where $F_{\chi_2^2}(x;\lambda)$ denotes the cumulative distribution function of a *non-central chi square* random variable with 2 degrees of freedom and *non-centrality parameter* λ.